

Perception through Scattering Media for Autonomous Vehicles

Nicolas Hautière¹, Raphaël Labayrade², Clément Boussard³,
Jean-Philippe Tarel¹, Didier Aubert⁴

¹ Laboratoire Central des Ponts et Chaussées,
Division Exploitation Signalisation Eclairage,
58 boulevard Lefebvre, 75015 Paris, France

² Ecole Nationale des Travaux Publics de l'Etat,
Direction Générale de la Construction et du Bâtiment,
rue Maurice Audin, 69120 Vaulx-en-Velin, France

³ Ecole Nationale Supérieure des Mines de Paris,
Centre de Robotique,
60-62 boulevard Saint Michel, 75006 Paris, France

⁴ Laboratoire sur les Interactions Véhicules Infrastructure Conducteurs,
unité mixte de l'INRETS et du LCPC,
bâtiment 824, 14 route de la Minière, 78000 Versailles, France

Abstract - The perception of the environment is a fundamental task for autonomous robots. Unfortunately, the performances of the vision systems are drastically altered in presence of bad weather, especially fog. Indeed, due to the scattering of light by atmospheric particles, the quality of the light signal is reduced, compared to what it is in clean air. Detecting and quantifying these degradations, even identifying their causes, should make it possible to estimate the operating range of the vision systems and thus constitute a kind of self-diagnosis system. In parallel, it should be possible to adapt the operation of the sensors, to improve the quality of the signal and to dynamically adjust the operation range of the associated processings. First, we introduce some knowledge about atmospheric optics and study the behavior of existing exteroceptive sensors in scattering media. Second, we explain how existing perception systems can be used and cooperate to derive some descriptors of the visibility conditions. In particular, we show how to detect fog presence and to estimate the visibility range. Once weather conditions have been determined, they can be exploited to reduce the impact of adverse weather conditions on the operation of vision systems. We propose thus different solutions to enhance the performances of vision algorithms

under foggy weather. Finally, we tackle the problem to know if light scattering could be turned to our advantage, allowing us to develop novel perception algorithms. Experiments in real situations are presented to illustrate the developments. Limits of the systems, future challenges and trends are discussed.

1 Introduction

Many factors can alter the quality of the signal resulting from an optical sensor mounted onboard an automotive vehicle (camera, laser, etc.): the fog, the rain, the sun at grazing angle, the reflections on the pavement, the presence of stains on the windshield, the glare due to the headlights of other vehicles, the strong gradients of brightness at the entrance and exit of tunnels, etc. To be able to detect and quantify these degraded operation conditions while relying only on the signals resulting from sensors themselves is a challenge for the future driver assistances based on optical sensors.

First, it is one of the keys to obtain a very important level of reliability of the sensor unit and associated signal processing. Indeed, whatever its intrinsic qualities, a processing will produce the awaited answers only if the input signal has a sufficient level of quality. Detecting and quantifying the degradations of this signal, even identifying the causes of these degradations, should make it possible to estimate an index of confidence on the operation of the system and thus constitute a kind of self-diagnosis system. In parallel, it can be possible to adapt the operation of the sensor, to improve the quality of the signal and/or to dynamically adjust some parameters in the processing.

Second, it is a means of carrying out new driver assistances, e.g. the automation of the fog lamps. This is also a means of gathering within the same sensor (in particular a camera) a set of functions that are already present in the vehicle (rain sensor, light level sensor) or that are going to come (automatic fog lamps, automatic demisting, automatic cleaning of the stains for example). Such a reduction of the number of sensors would make it possible to decrease the volume and the total cost of the system.

Third, some of the causes of the degradation of the signal quality are also causes of road accidents (e.g. rain, fog, sun at grazing angle, etc.). Thus, by establishing a mapping function between the vision of the driver and the vision of the sensor, in particular in terms of dynamic range, resolution and sensitivity, such algorithms can make it possible to generate relevant alarms for the driver in the event of behaviors unsuited to the traffic conditions.

Until now, this approach has been followed for the computation of the visibility range, which constitutes a relevant and illustrative case study. Starting from existing works on fog modeling, two complementary methods have been developed aiming at estimating the visibility range using respectively one or two onboard cameras. Both methods are based on the definition of the meteorological visibility distance. The first technique, using a model of atmospheric scattering, detects and estimates the density of daytime fog by using a single camera. The second technique, using a generic property of the atmosphere, is able to estimate the visibility range under all meteorological conditions both in daytime and in night time by using a stereoscopic sensor or a single camera coupled with an inertial navigation

system. In the future, these methods are likely to be used to provide drivers with an appropriate speed with respect to the visibility range, to enhance obstacle detection techniques or to automate the fog lamps.

This paper is organized as follows. First, it deals with the general problem of artificial perception under adverse weather conditions. Second, both approaches computing the visibility range are presented and validated thanks to actual images and video sequences grabbed under various situations on the test track of Versailles Satory. In particular, we show how to detect fog presence. We propose then different solutions to enhance the performances of vision algorithms under foggy weather. Finally, some ideas for future researches are indicated.

2 Vision and the Atmosphere

The literature on the interaction of light with the atmosphere has been written over more than two centuries [1, 8]. Different reviews on the topic have been available in the literature [45, 46] for half a century and still serve as reference for recent works in computer vision.

2.1 Fog Characteristics

2.1.1 Definition

Fog is a thick cloud of microscopic water droplets suspended at ground level. When the horizontal visibility is smaller than 1 km, one speaks about fog. When the horizontal visibility is greater than 1 km, one speaks rather about haze. The fog is usually characterized by two parameters: the granulometry and the concentration of water droplets.

2.1.2 Light propagation through fog

In a schematic way, the visible light must go through an aerosol which contains a great number of particles having a diameter of a few micrometers. The wavelength of visual light is comprised between 400 nm and 700 nm.

When light propagating in fog, the luminous flow is attenuated by two phenomena: absorption and scattering, which leads to characterize fog by an extinction coefficient k , which is the sum of the absorption and scattering coefficients. In fact for visible light, absorption is negligible in this type of aerosol. The main phenomena in the light attenuation is thus scattering which deviates light rays from their initial direction. Finally, fog is characterized by an extinction coefficient k which is equal to the scattering coefficient.

If ϕ_0 is the luminous flow emitted by a given light source, the transmitted flow ϕ along the distance d through fog is given by Beer-Lambert's Law:

$$\phi = \phi_0 e^{-kd} \quad (1)$$

where the product kd represents the optical thickness of the scattering media.

2.2 Fog visual effects

In the preceding paragraph, we have defined the physical characteristics of fog and the resulting phenomena, i.e. the visible light scattering. Based on [20], we propose in this paragraph to describe the different visual effects of this phenomena. We focus mainly on daytime fog situations.

2.2.1 Attenuation

During daytime, the sky is the main source of luminous energy. It generates a uniform illuminance throughout the environment, which depends on time as well as geographical and meteorological conditions. Part of this energy is re-emitted toward the camera, generating an intrinsic luminance L_0 . In the presence of fog, part of this energy is scattered by fog along the distance d between a scene element and the camera, causing the transmitted luminance L_t to be attenuated by a factor equal to e^{-kd} :

$$L_t = L_0 e^{-kd} \quad (2)$$

2.2.2 Halo effect

Fog alters the visual signal by scattering the light emitted by every light source. Part of this energy is scattered back towards the camera off-axis, adding a halo of scattered light around the transmitted signal. This effect was shown to be equivalent to a convolution. Therefore, by analogy with an optical filter, a slab of fog can be characterized with its modulation transfer function (MTF), equal to the module of the Fourier transform (FT) of its point spread function (PSF). Halo effect is negligible under daytime conditions, contrary to nighttime situations like in Fig. 1b.

2.2.3 Veiling effects

Veil from Atmosphere In daytime fog, the droplets in the air between the observer and the elements of the road environment also contribute to the apparent luminance by scattering toward the eye some of the energy it receives from the sky (single scattering) and from other droplets (multiple scattering). The resulting luminance L_a known as the atmospheric veiling luminance or airlight increases exponentially with distance (cf. Fig. 1a):

$$L_a = (1 - e^{-kd})L_f \quad (3)$$

where L_f denotes the luminance of the fog at the horizon.

Veil from Backscattering When the observer is driving in fog, the low-beam headlamps of his vehicle ought to be turned on. Fog droplets in front of the vehicle interact with this luminous flux, scattering a part of it back into the eyes of the driver in a nonuniform luminance distribution, known as the backscattered veiling luminance. It was found to be at

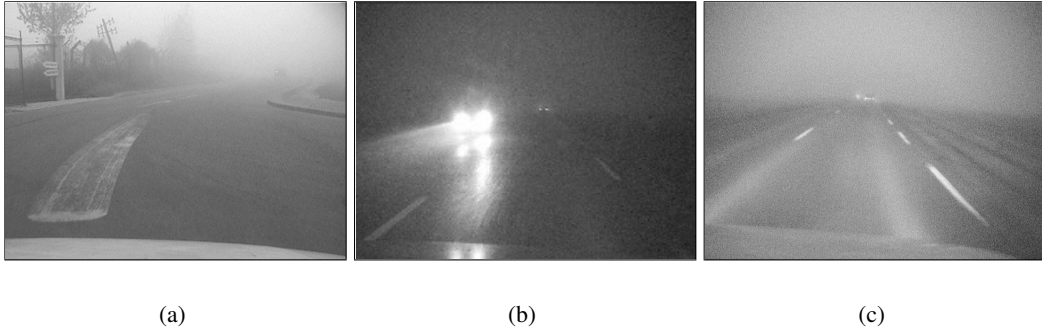


Figure 1: Illustration of fog effects on vision: (a) atmospheric veil; (b) halo; (c) backscattered veil.

least two orders of magnitude smaller than the atmospheric veiling luminance in daytime. Yet, it contributes to the loss of visibility in nighttime conditions and therefore should be taken into account (cf. Fig. 1c).

2.3 Modeling Fog Visual Effects

In 1924, Koschmieder [45] established a simple relationship between the apparent luminance L of an object at a distance d , and its intrinsic luminance L_0 :

$$L = L_0 e^{-kd} + L_f (1 - e^{-kd}) \quad (4)$$

where L_f denotes the luminance of background sky. Based on these results, Duntley [45] derived a law for the atmospheric attenuation of contrasts:

$$C = \frac{|L - L_f|}{L_f} = C_0 e^{-kd} \quad (5)$$

where C designates the apparent contrast at distance d and C_0 the intrinsic contrast of the object against the sky.

The CIE [16] adopted a contrast threshold of 5% to define V_{met} , the "meteorological" visibility distance, defined as the greatest distance at which a black object ($C_0 = -1$) of suitable dimensions can be recognized by day against the horizon sky:

$$V_{met} = -\frac{1}{k} \log(0.05) \simeq \frac{3}{k} \quad (6)$$

An extended model of fog taken into account all the different effects has been proposed in [20]. However, in this chapter, we focus on daytime situations, where despite its limitations, Koschmieder's model has been proven to be very useful.

3 Recovering the Extinction Coefficient of Fog

The operation range of exteroceptive sensors depends on the weather conditions. A study has been done in [36] to evaluate the operation range of infrastructure based sensors with respect to weather conditions. The results can be extrapolated for in-vehicle sensors. Thus, according to the curves plotted in Fig. 2 and partially extracted from [5], the output signal of optical sensors running in the visible or near infrared light range is degraded by adverse weather conditions. Consequently, signal processings techniques relying on optical sensors to detect obstacles or the lane markings are less efficient under adverse weather conditions.

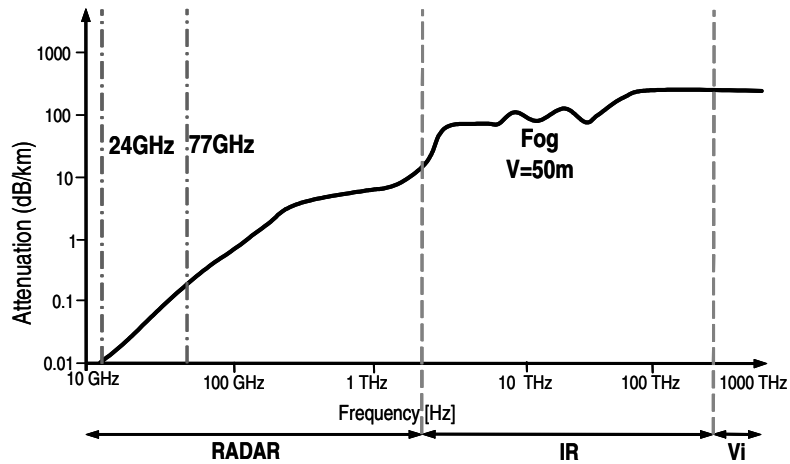


Figure 2: Curve, partially issued from [5], depicting the atmospheric attenuation due to dense fog ($V=50$ m) according to the frequency of the signal.

Thus we may use optical sensors to characterize fog and in particular to recover the value of the atmospheric extinction coefficient k . In this paragraph, we review the different approaches which have been published.

3.1 Road Visibilitymeters

This lexicographical term serves to designate two main types of instruments for both detecting fog and measuring the extinction coefficient k ; they are transmissometers and scatterometers [42].

3.1.1 Transmissometers

The basic principle behind this category of instrument consists of measuring average transmissivity of the atmosphere along a given path (see Fig. 3). Transmissometers are composed of both a projector comprising a source emitting a luminous flux ϕ_0 within the visible

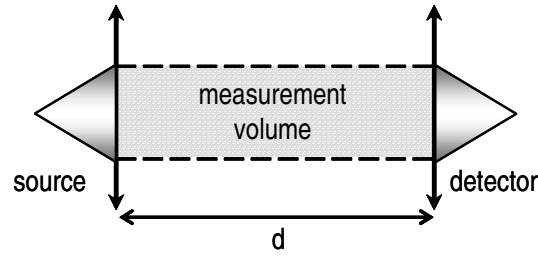


Figure 3: The operating principle of a transmissometer is to measure the average transmissivity of the atmosphere along a given path.

domain and a receiver set located at an invariable distance d that measures the luminous flux ϕ received.

By using Beer-Lambert's Law, the extinction coefficient of the fog k , used for calculating the meteorological visibility distance (6), is given by:

$$k = \frac{1}{d} \log \left[\frac{\phi}{\phi_0} \right] \quad (7)$$

The transmissometers are reliable. Their sensitivity is related to the length of the measurement base d . This length, which extends over several meters or even several tens of meters, provides these devices with a high level of accuracy, given the lack of homogeneity often encountered in fog. Transmissometers however are costly to implement and the optical block alignment frequently proves to be a complex procedure.

3.1.2 Scatterometers

Some of these devices were developed for road applications, primarily for conducting measurements under conditions of thick fog. They enable quantifying the light diffused within a sufficiently wide and well-defined solid angle. In order to carry out such measurements, a light beam is concentrated on a small volume of air (see Fig. 4). The proportion of light being diffused toward the receiver would then be:

$$I = AI_0 V f(\theta) e^{-kd} \quad (8)$$

with I the intensity diffused in the direction of the receiver, A a constant dependent on power and source optics, I_0 the source intensity, V the diffusing volume, $f(\theta)$ the value of the diffusion function in the θ direction, k the extinction coefficient and d the length of the optical path between emitter and receiver.

Generally speaking, the optical path d is small and the transmission factor e^{-kd} is assimilated to 1 and $f(\theta)$ is proportional to k , with (8) thereby becoming:

$$I = A' I_0 k, \text{ then } k = \frac{1}{A'} \frac{I}{I_0} \quad (9)$$

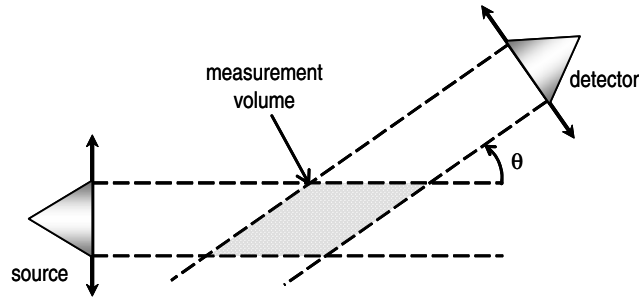


Figure 4: The operating principle of a scatterometer is to measure the light diffused in a well-defined solid angle.

where A' designates a constant that depends on device characteristics.

We can state that a scatterometer, to its advantage, is significantly less expensive than a transmissometer and that no optical block alignment is required. On the other hand, the small size of the diffusing volume makes measurements highly sensitive to non-homogeneities in the fog. Furthermore, the sensor accuracy decreases with the meteorological visibility and is not acceptable for visibilities below 50m.

Consequently, neither a transmissometer or a scatterometer may be easily placed on-board a moving vehicle. Indeed, the measurement path is too short and the alignment of optical blocks is difficult for a transmissometer. A scatterometer would be too sensitive to the turbulence caused by the motion of the vehicle. However, it would be interesting to make some trials.

3.2 LIDAR

This laser based sensor can be used for estimating fog density by measuring the signal backscattered by fog droplets [11]. The power per pulse from range r received by a LIDAR is given by the simplified LIDAR equation [17]:

$$P_R(r) = \frac{P_T c \tau \beta A_e}{8\pi r^2} \exp \left[-2 \int_0^r k(x) dx \right] \quad (10)$$

where P_T denotes the peak transmitted power per pulse, c the speed of light, τ the pulse duration, β the backscatter cross section per unit volume, A_e the effective receiver aperture and $k(x)$ the atmospheric extinction coefficient.

Under strictly homogeneous conditions, β and k are not dependant of range. Hence, (10) becomes:

$$P_R(r) = \frac{A''}{r^2} \exp[-2kr] \quad (11)$$

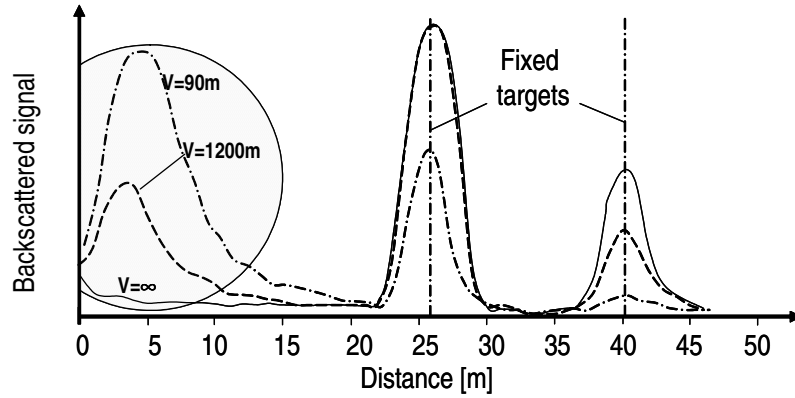


Figure 5: Plot of the backscattered signal by a LIDAR in the presence of artificial fog based on [7]. The diagram also shows the detection of two fixed targets.

where A'' denotes a constant that depends on device characteristics. The slope of the decaying waveform when differentiating (10) with respect to range becomes:

$$\frac{dP_R(r)}{dr} = P_R(r) \left[-2k - \frac{2}{r} \right] \quad (12)$$

This differential equation is the basic principle on which the LIDAR measurement of the extinction coefficient in a homogeneous scattering medium is done (cf. Fig. 5).

For automotive applications, the LIDAR seems to be the best suited *active* sensor for estimating the meteorological visibility, since it does not need any external receiver, contrary to infrastructure based visibility meters, and can be used for other safety applications, e.g. obstacles detection [51] or lane recognition [49]. Consequently, it has been used for adjusting the power of headlights [7, 54] or for adjusting the headway in Automatic Cruise Control (ACC) [13] according to the prevailing meteorological conditions. However, it has been shown that the dynamic adaptation of the emitting power of a LIDAR with respect to visibility conditions is not always perfect [18].

3.3 Camera

If a camera is used, there is no need to align the optical units as it is the case with the transmissometer, and an image is obtained which is representative of the environment, unlike with a scatterometer. Finally, in the case of a classical camera, the spectra taken into account is in the visible domain. Consequently, its image is degraded by the presence of fog. Most approaches make use of a fixed camera placed on the roadway which simplifies the task as a reference image is always available [12, 37].

Systems that entail use of an onboard camera are encountered less frequently. Pomerleau [53] estimates visibility by means of measuring a contrast attenuation per meter on the

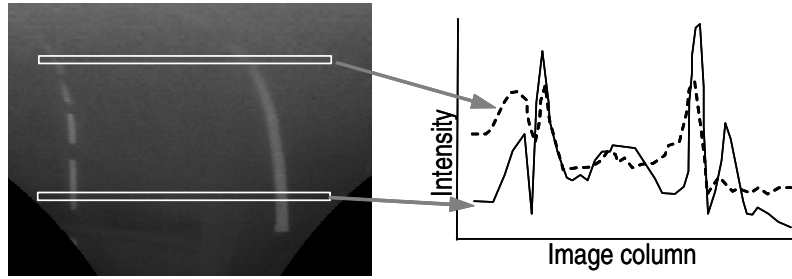


Figure 6: Principle of the approach proposed in [53] to estimate the visibility distance based on lane markings contrast attenuation.

road markings at various distances in front of the vehicle. However, this approach based on the RALPH System [52] only indicates a relative visibility distance and requires the detection of road markings to run. The principle of the technique is schematized in Fig. 6.

Yahiaoui [61] estimates the quality of images by comparing the MTF of the current image with a contrast sensitivity function [44]. However, it only returns a potential visibility distance. So, these methods estimate what could be the maximum visibility distance in the scene.

In the two next sections, we present our camera based approaches. The first is able to estimate the extinction coefficient of the atmosphere using a single camera. The second is able to estimate the actual visibility range using either a camera coupled with an Inertial Navigation System (INS) or with a binocular camera.

4 Automatic Fog Detection and Estimation of the Meteorological Visibility Distance

In this section, a method to compute the extinction coefficient k and thus the meteorological visibility distance using a single camera behind the vehicle windshield is recalled from [32]. This system was patented [41].

4.1 Flat World Hypothesis

In the image plane, the position of a pixel is given by its (u, v) coordinates. The coordinates of the optical center projection in the image are designated by (u_0, v_0) . In Fig. 7, H denotes the height of the camera, θ the angle between the optical axis of the camera and the horizontal, and v_h the horizon line. The intrinsic parameters of the camera are its focal length f_l , and the horizontal size t_{pu} and vertical size t_{pv} of a pixel. We have also made use herein of $\alpha_u = \frac{f_l}{t_{pu}}$ and $\alpha_v = \frac{f_l}{t_{pv}}$, and have typically considered: $\alpha_u \approx \alpha_v = \alpha$. The road is assumed flat, which makes it possible to associate a distance d with each line v of the image:

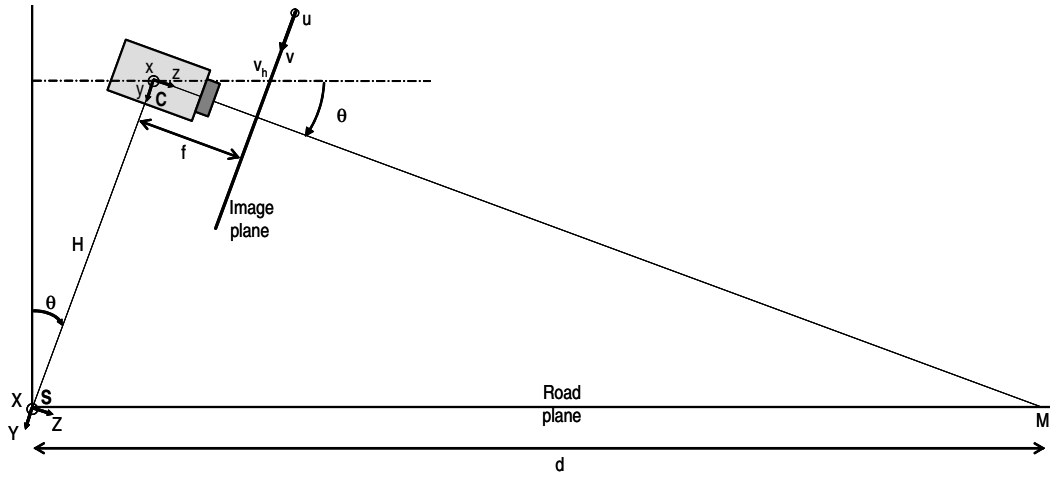


Figure 7: Modeling of the camera within its environment; it is located at a height of H in the (S, X, Y, Z) coordinate system relative to the scene. Its intrinsic parameters are its focal length f and pixel size t . θ is the angle between the optical axis of the camera and the horizontal. Within the image coordinate system, (u, v) designates the position of a pixel, (u_0, v_0) is the position of the optical center C and v_h is the vertical position of the horizon line.

$$d = \frac{\lambda}{v - v_h} \quad \text{if } v > v_h, \quad \text{where } \lambda = \frac{H\alpha}{\cos \theta} \quad (13)$$

4.2 Camera Response

Let us denote f the camera response function, which models the mapping from scene luminance to image intensity by the imaging system, including optic as well as electronic parts [22]. With the notations of Section 2, the intensity I of a pixel is the result of f applied to the sum of the airlight L_a and the direct transmission L_t , i.e:

$$I = f(L) = f(L_t + L_a) \quad (14)$$

In this work, we assume that the conversion process between incident energy on the CCD sensor and the intensity in the image is linear. This is generally the case for short exposure times, because it prevents CCD array to be saturated. Furthermore, short exposure times (1 to 4 ms) are used on in-vehicle cameras to reduce the motion blur. This assumption can thus be considered as valid and (14) becomes:

$$\begin{aligned} I &= f(L_t) + f(L_a) = f(L_0 e^{-kd}) + f[L_f(1 - e^{-kd})] \\ &= f(L_0) e^{-kd} + f(L_f)(1 - e^{-kd}) \\ &= R e^{-kd} + A_\infty(1 - e^{-kd}) \end{aligned} \quad (15)$$

where R is the intrinsic intensity of the pixel, i.e. the intensity corresponding to the intrinsic luminance value of the corresponding scene point and A_∞ is the background sky intensity.

4.3 Recovery of Koschmieder's Law Parameters

Following a variable change from d to v based on (13), (15) then becomes:

$$I(v) = R - (R - A_\infty)(1 - e^{-\frac{k\lambda}{v-v_h}}) \quad (16)$$

By twice taking the derivative of I with respect to v , one obtains the following:

$$\frac{d^2I}{dv^2}(v) = k\varphi(v)e^{-\frac{k\lambda}{v-v_h}} \left(\frac{k\lambda}{v-v_h} - 2 \right) \quad (17)$$

where $\varphi(v) = \frac{\lambda(R-A_\infty)}{(v-v_h)^3}$. The equation $\frac{d^2I}{dv^2} = 0$ has two solutions. The solution $k = 0$ is of no interest. The only useful solution is given in (18):

$$k = \frac{2(v_i - v_h)}{\lambda} \quad (18)$$

where v_i denotes the position of the inflection point of $I(v)$. In this manner, the parameter k of Koschmieder's law is obtained once v_i is known. Finally, thanks to v_i , v_h and k values, the values of the other parameters of (15) are deduced through use of I_i and $\frac{dI}{dv}|_{v=v_i}$, which are respectively the values of the function I and of its first derivative at $v = v_i$:

$$R = I_i - (1 - e^{-kd_i}) \frac{(v_i - v_h)}{2e^{-kd_i}} \frac{dI}{dv} \Big|_{v=v_i} \quad (19)$$

$$A_\infty = I_i + \frac{(v_i - v_h)}{2} \frac{dI}{dv} \Big|_{v=v_i} \quad (20)$$

where R is the mean intrinsic intensity of the road surface.

4.4 Implementation

4.4.1 Estimation of the inflection point position

To estimate the parameters of (15), the median intensity on each line of a vertical band is estimated and an inflection point is detected. So as to be in accordance with Koschmieder's law assumptions, this band should only take into account a homogeneous area and the sky. Thus, a region within the image that displays minimal line-to-line gradient variations when browsed from bottom to top is identified thanks to a region growing process, illustrated in Fig. 8a. A vertical band is then selected in the detected area. Finally, taking the median intensity of each segment, yields the vertical image intensity \tilde{I} from which the inflection point is computed.

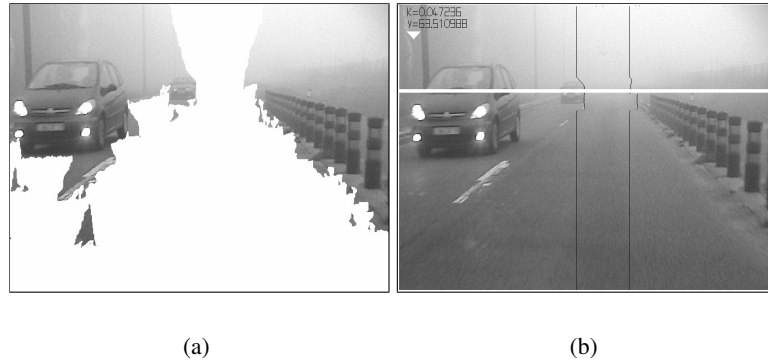


Figure 8: (a) Detection of the road and the sky by a region growing process; (b) the horizontal white line represents the estimation of the visibility distance. The small white triangle on the image top left indicates that the system is operative. Conversely, a small black triangle indicates that the system is temporarily inoperative. The black vertical lines represent the limits of the vertical band analyzed. In this example, $V_{met} \approx 60\text{m}$.

4.4.2 Estimation of the horizon line position

To obtain the values of the parameters of (15), the position of the horizon line must be estimated. It can be estimated by means of the pitching of the vehicle when an inertial sensor is available, but is generally estimated by an additional image processing. Generally, this type of processing seeks to intersect the vanishing lines in the image. However, under foggy weather, the vanishing lines are only visible close to the vehicle. It is thus necessary to extrapolate the position of the horizon line through the fog. Consequently, this kind of process is prone to a significant standard deviation and, for the moment, we use the a priori sensor calibration.

Having now the vertical positions of both the inflection point and the horizon line, the parameters of (15) can be recovered and the position of the image line representative of the meteorological visibility distance is deduced. Fig. 8b illustrates the process.

4.5 Confidence Index on the Measurement

Given that we have a theoretical model of the vertical variation of the intensity in the image, the confidence index on the measurement is linked with the difference between the theoretical model I and its estimation \tilde{I} . In other words, the more noisy \tilde{I} is, the less reliable the measurement is. Let us quantify this difference. As the theoretical curve is decreasing, we first smooth \tilde{I} until it becomes decreasing. We denote this curve \bar{I} . We then compute the difference E between the derivative of \tilde{I} and the derivative of \bar{I} , which can be expressed as following:

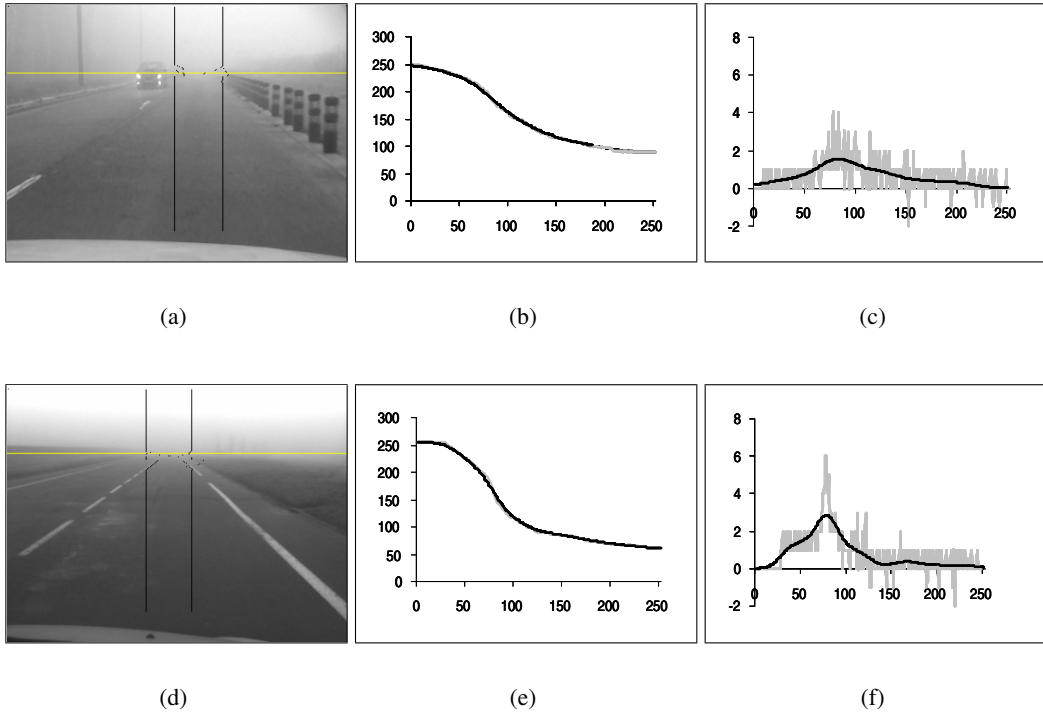


Figure 9: Examples of measurement bandwidth computations (black lines) under foggy conditions: (a) low fog density, and (d) high density. Curves representative of the measurement of vertical luminance variation in the image under foggy conditions: (b) low fog density, and (e) high density. (c) and (f) depict the derivatives of these curves (gray - without smoothing \tilde{L} ; black - with smoothing \bar{L}) and allows to compute C , respectively equal to 86% and 91%.

$$E = \sum_{i=1}^n \left| \frac{\partial \tilde{I}}{\partial v}(i) - \frac{\partial \bar{I}}{\partial v}(i) \right| \quad (21)$$

The maximum error E_{max} which can be made on the computation of the derivative is equal to:

$$E_{max} = n \times G_{max} \quad (22)$$

where G_{max} denotes the maximum authorized value of the vertical gradient in the region growing process and n the lines number of the measurement bandwidth. A normalized confidence index C can be formulated:

$$C = \frac{E_{max} - E}{E_{max}} \quad (23)$$

The proposed index has been validated using synthetic data. Two examples of index confidence computations are given in Fig. 9.

4.6 Analysis of the Method Sensitivity

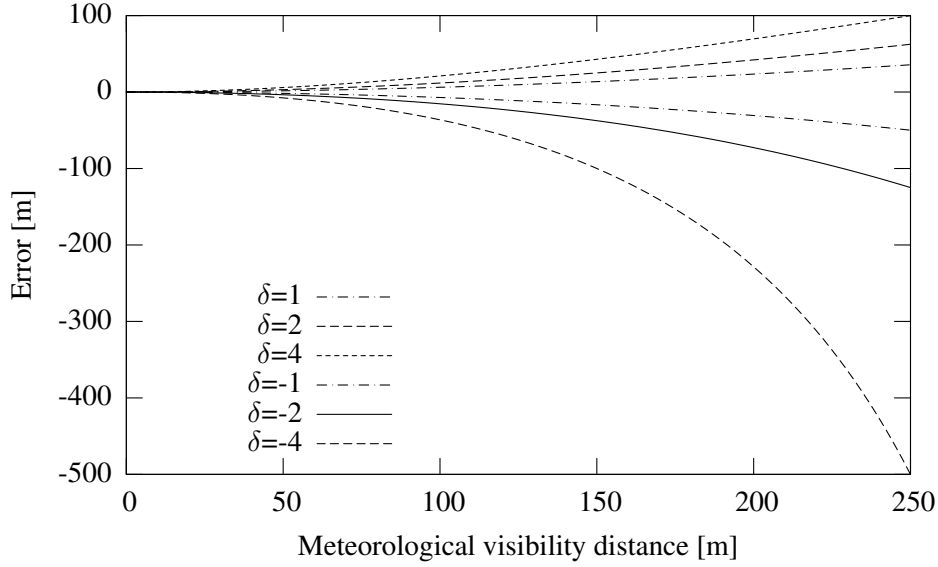


Figure 10: Method sensitivity with respect to δ value. Used parameter: $\lambda = 1000$.

The estimation of V_{met} is correct if the position v_i of the inflection point as well as the position v_h of the horizon line are correct. Let us study the influence of an estimation error δ on the difference of these two positions. The error S between the estimated meteorological visibility distance \tilde{V}_{met} and the actual meteorological visibility distance V_{met} is expressed with respect to δ value by:

$$\begin{aligned}
 S &= V_{met} - \tilde{V}_{met} \\
 &= V_{met} - \frac{3\lambda}{2} \frac{1}{v_i - v_h + \delta} \\
 &= V_{met} \left[1 - \frac{1}{1 + \frac{2\delta V_{met}}{3\lambda}} \right]
 \end{aligned} \tag{24}$$

The curves in Fig. 10 give the committed error for values of δ ranging from -4 to +4. We can conclude that underestimate the difference of positions is more penalizing than overestimate it. To have stable measurements, we thus prefer set the horizon line above its real position.

Figs. 11 and 12 show some results of meteorological visibility distance computations in two daytime fog video sequences.

4.7 Extension of the Method

4.7.1 Masking problem

To run properly, the previous method needs a homogeneous area and the sky. In case of a low dense fog or a strong masking of the road, the method is not operative anymore. Indeed, the region growing is unable to cross the image from bottom to top. Figs. 13abc show such situations.

4.7.2 Complementary approach

To limit the problem, when it is possible, we propose to add a measurement of the contrast attenuation between the road and the lane markings [23], like it was proposed in [53]. However, in our case, instead of directly detecting the markings, we prefer using the results of the previous region growing. In this aim, we assume that the markings are on the border of the area detected by the region growing algorithm and we search the pixels whose intensity is greater than the median intensity I_m of the considered image line. Then, on each line, the median intensity I_M of the lane markings is computed. Some examples are shown in Fig. 14. In fact, this approach could be used under every meteorological conditions. However, under beautiful weather, the shadows prevent the method to run properly contrary to foggy weather where there is no shadows.

Thereafter, contrary to [53] who estimates a contrast attenuation factor per meter, we prefer to estimate the meteorological visibility distance so as to be coherent between both methods. Thanks to (4), we know the theoretical variations of I_m (road intensity) and I_M (markings intensity) with respect to the distance. By considering two distances d_1 and d_2 , the extinction coefficient k can be expressed by:

$$k = \frac{1}{d_2 - d_1} \log \left[\frac{I_{M_1} - I_{m_1}}{I_{M_2} - I_{M_1}} \right] \quad (25)$$

We deduce the value of the meteorological visibility distance as:

$$V_{met} = \frac{3(d_2 - d_1)}{\log \left[\frac{I_{M_1} - I_{m_1}}{I_{M_2} - I_{M_1}} \right]} \quad (26)$$

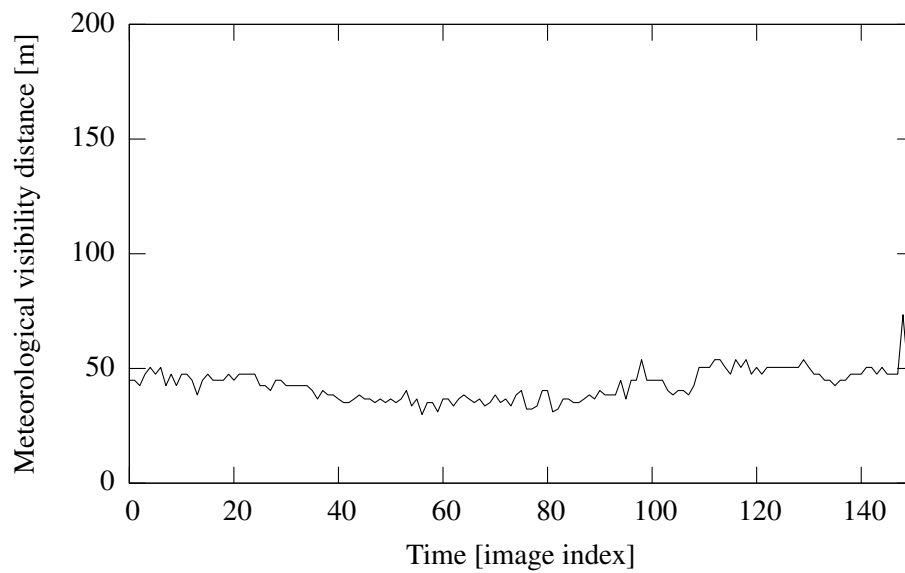
Both methods are complementary. Whereas the first method does not need the presence of road markings, the second one does not need the presence of the sky in the image. It is thus possible to draw advantage from both methods to build a better one.



(a)

(b)

(c)



(d)

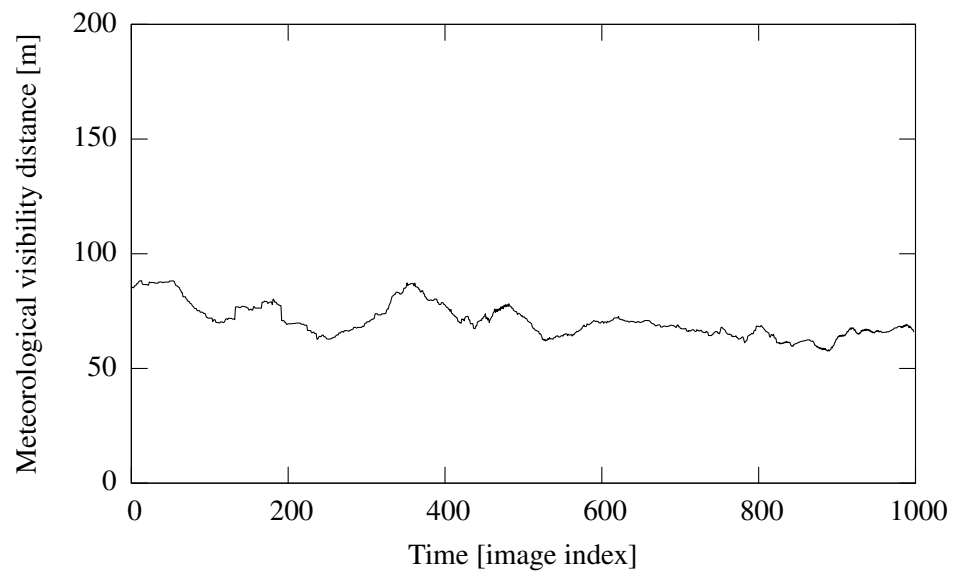
Figure 11: (d) Plot of the meteorological visibility distance estimation based on the daytime fog video sequence illustrated in (a)(b)(c).



(a)

(b)

(c)



(d)

Figure 12: (d) Plot of the meteorological visibility distance estimation based on the daytime fog video sequence illustrated in (a)(b)(c).

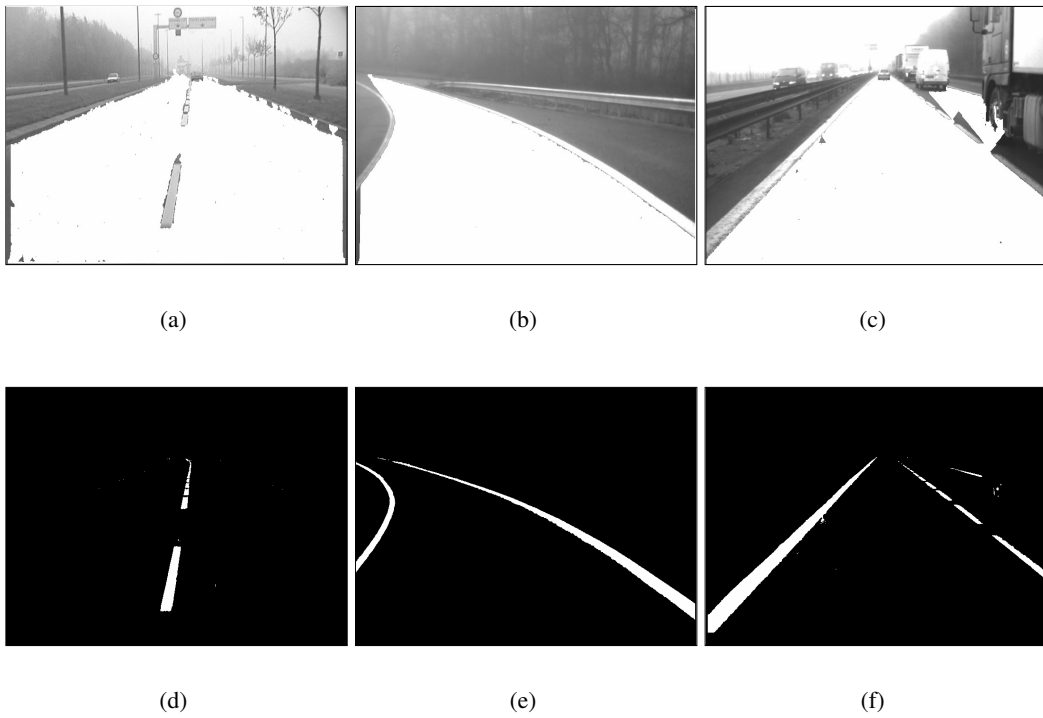


Figure 13: (a)(b)(c) Examples where the region growing algorithm is not successful due to the masking of the road; (d)(e)(f) Lane markings detection based on the region growing algorithm.

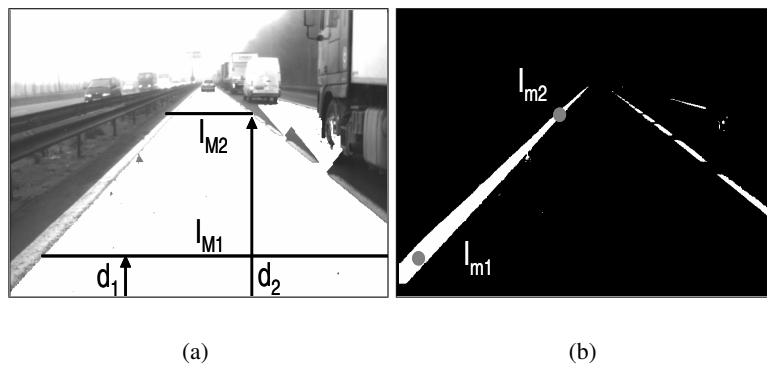


Figure 14: Estimation of the meteorological visibility distance based on the lane markings contrast attenuation.

5 Estimation of the Visibility Distance: a Generic Approach

The previous method leads to good results in daytime foggy weather. In order to extend the range of covered meteorological situations, we developed a different approach, which consists in estimating what we call the mobilized visibility distance V_{mob} [25].

5.1 Generic Method Proposal

5.1.1 Mobilized Visibility Distance

For the CIE, the meteorological visibility distance is the greatest distance at which a black object of a suitable dimension can be seen in the sky on the horizon. We have decided to build a method which is close to this definition. In this aim, we propose to study the distance to the most distant object having enough contrast with respect to its background.

On Fig. 15, we represent a simplified road with dash road marking. On Fig. 15a, we suppose that the most distant visible object is the extremity of the last road marking (it could have been the border of the road too). On Fig. 15b, the vehicle has moved and a new road marking is now visible. We call this distance to the most distant visible object, which depends on the road scene, the mobilized visibility distance V_{mob} . This distance has to be compared to the mobilizable visibility distance V_{max} . This is the greatest distance at which a picture element on the road surface would be visible.

Consequently, we have the following relationship:

$$V_{max} \geq V_{mob} \quad (27)$$

5.1.2 Mobilizable Visibility Distance

In this section, we are going to establish the link between the mobilizable visibility distance and the meteorological visibility distance. The mobilized visibility distance is the distance to the most distant object W considered as visible. We denote L_{b_0} and L_{w_0} , the intrinsic luminances and L_b et L_w the luminances at the distance d of the road B and the object W .

Koschmieder's law gives us the theoretical variations of this values according to the distance d . Let's express the contrast C_{BW} of W with respect to B like Weber does, see (36):

$$C_{BW} = \frac{\Delta L}{L} = \frac{(L_{w_0} - L_{b_0})e^{-kd}}{L_{b_0}e^{-kd} + L_f(1 - e^{-kd})} \quad (28)$$

We deduce the expression of d according to the photometric parameters, the contrast C_{BW} and the fog density k :

$$d = -\frac{1}{k} \log \left[\frac{C_{BW}L_f}{L_{w_0} - L_{b_0} + C_{BW}(L_f - L_{b_0})} \right] \quad (29)$$

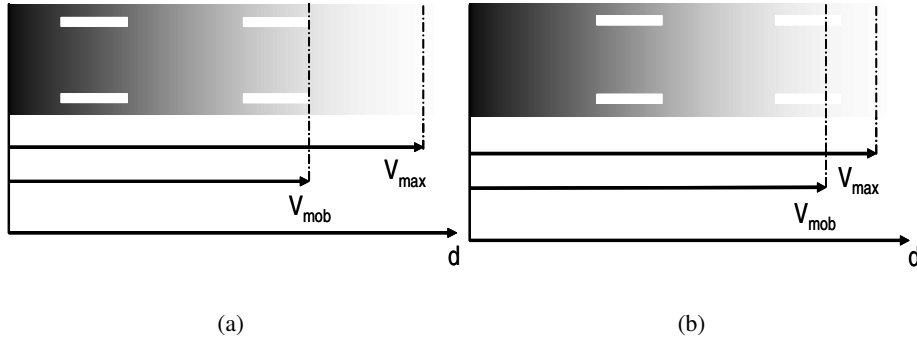


Figure 15: Examples of mobilized and mobilizable visibility distances. The mobilized visibility distance V_{mob} is the distance to the most distant visible object existing on the road surface. The mobilizable visibility distance V_{max} is the greatest distance at which a potential object on the road surface would be visible.

That is to say the distance where an object W is perceived with a contrast of C_{BW} . Thanks to (6), we can express this value according to the meteorological visibility distance V_{met} :

$$d = -\frac{V_{met}}{3} \log \left[\frac{C_{BW} L_f}{L_{w_o} - L_{b_o} + C_{BW} (L_f - L_{b_o})} \right] \quad (30)$$

Like CIE does, we can choose a threshold \tilde{C}_{BW} below which the object is considered as being not visible. Like for the computation of the meteorological visibility distance, we assume that the road intrinsic luminance is equal to zero. Then, we define the mobilizable visibility distance V_{max} valid for every threshold contrast:

$$V_{max} = \max_{L_{w_o} \in]0, M]} -\frac{V_{met}}{3} \log \left[\frac{\tilde{C}_{BW} L_f}{L_{w_o} + \tilde{C}_{BW} L_f} \right] \quad (31)$$

The energy received by the object W is not entirely reflected towards the camera. Consequently, we have the following relationship:

$$L_{w_o} \leq L_f \quad (32)$$

We deduce the value of V_{max} :

$$V_{max} = -\frac{V_{met}}{3} \log \left[\frac{\tilde{C}_{BW}}{1 + \tilde{C}_{BW}} \right] \quad (33)$$

Then, we easily obtain the value \tilde{C}_{BW} so that $V_{max} = V_{met}$:

$$\tilde{C}_{BW} = \frac{1}{e^3 - 1} \approx 5\% \quad (34)$$

So, by choosing a contrast threshold \tilde{C}_{BW} of 5 %, the mobilizable visibility distance is close to the meteorological visibility distance V_{met} for a black object.

Actually, the road is never pure black and the sky rarely pure white. The mobilizable visibility distance represents a maximum of visibility distance which is rarely reachable, since it is the greatest distance at which the clearest object is visible on a black road. On the other hand, the mobilized visibility distance, which only takes into account the gray objects encountered in the image is the distance that we are able to estimate directly as explained in the following.

5.1.3 Proposed Method

In section 5.1.1, we have introduced the concepts of mobilized and mobilizable visibility distances. Whereas the first one depends on the road scene, the second one only depends on the meteorological conditions. Then, in section 5.1.2, we established the link between the meteorological visibility distance defined by the CIE and the mobilizable visibility distance previously defined. In particular, we calculated the contrast threshold so that both distances are the same, that is to say 5 %. Consequently, we propose to estimate the mobilized visibility distance by estimating the distance to the most distant object on the road surface having a contrast above 5 %. This method is decomposed in two tasks. The first one consists in computing the contrasts in the image and selecting the ones above 5 %. The second one is the depth computation of the detected picture elements and the selection of the most distant one.

5.2 The Measurement of Contrast

5.2.1 Contrast and digital images

Different definitions of the contrast exist. One of the most famous is Michelson's contrast [60]. It has been introduced to quantify the visibility of sinusoidal gratings:

$$C^M = \frac{L_{max} - L_{min}}{L_{max} + L_{min}} \quad (35)$$

where L_{min} and L_{max} are the minimal and maximum luminance values of the image. The use of sinusoidal gratings and of this contrast definition has met a great success in psychophysics. In particular, it has been used to study the human eye by building contrast sensivity functions (CSF).

Weber [60] defined the contrast as being a relative luminance variation ΔL with respect to the background L . This has been used to measure the visibility of targets:

$$C^W = \frac{\Delta L}{L} \quad (36)$$

This contrast definition is sometimes called psychophysical contrast and it is used in the definition of the meteorological visibility distance.

These definitions are good estimators of contrast for the stimuli previously mentioned: sinusoidal gratings for Michelson, uniform targets for Weber. However, they are not well adapted when the stimulus becomes more complex. Moreover, none of these definitions are adapted to estimate the contrast in natural images. This is mainly due to the fact that the contrast perception is local. This is on these local methods that we focused our attention.

The LIP model [35] has introduced a definition of contrast well suited to digital images. In this definition, the contrast between two pixels x and y of an image f is given by:

$$C_{(x,y)}(f) = \max[f(x), f(y)] \triangle \min[f(x), f(y)] \quad (37)$$

where \triangle denotes LIP subtraction. Naturally, this definition of contrast is consistent with the definition of contrast used in visual perception (36).

Then, the contrast associated to a border F which separates two adjacent regions follows:

$$C_F(f) = \frac{1}{\text{card } V} \triangle \bigtriangleup_{(x,y) \in V} C_{(x,y)}(f) \quad (38)$$

where \bigtriangleup and \triangle denote LIP multiplication and addition.

5.2.2 Implementation

To implement this definition of contrast between two adjacent regions, Köhler's segmentation method has been used [38]. Let f be a gray level image. A couple of pixels (x,y) is said to be separated by the threshold s if two conditions are met. First, $y \in V_4(x)$. Secondly, the condition (39) is respected:

$$\min [f(x), f(y)] \leq s < \max [f(x), f(y)] \quad (39)$$

Let $F(s)$ be the set of all couples (x,y) separated by s . With these definitions, for every value of s belonging to $[0,255]$, $F(s)$ is built. For every couple belonging to $F(s)$, the contrast $C_{x,y}(s)$ is computed:

$$C_{x,y}(s) = \min \left[\frac{|s - f(x)|}{\max(s, f(x))}, \frac{|s - f(y)|}{\max(s, f(y))} \right] \quad (40)$$

The mean contrast (41) associated to $F(s)$ is then performed:

$$C(s) = \frac{1}{\text{card } F(s)} \sum_{(x,y) \in F(s)} C_{x,y}(s) \quad (41)$$

The best threshold s_0 verifies the following condition:

$$s_0 = \operatorname{argmax}_{s \in [0,255[} C(s) \quad (42)$$

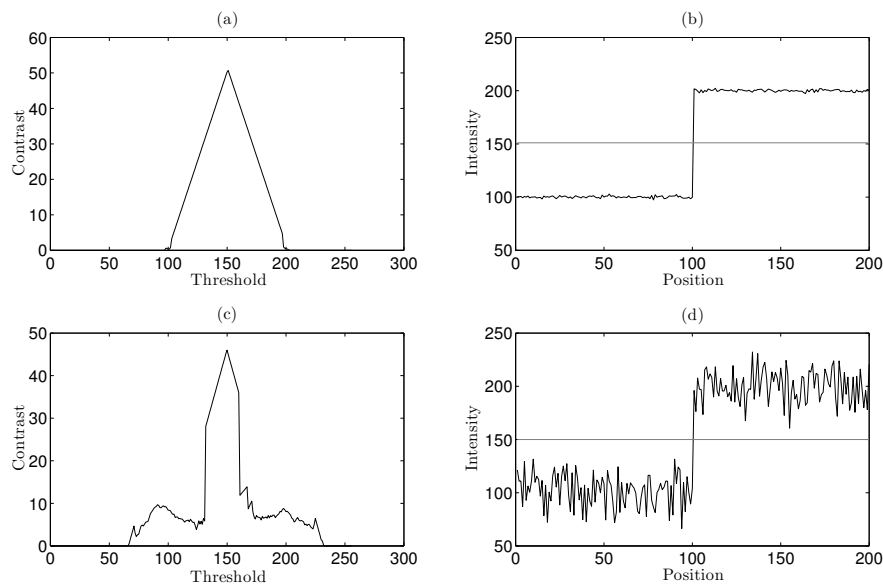


Figure 16: Noise robustness of Köhler's method adapted to the LIP contrast. One-dimensional edge modified by gaussian noise (b) $\sigma = 1$, (d) $\sigma = 15$. The dotted line represents the optimal threshold found by the method. The mean contrast $C(s)$ associated to each threshold value s is plotted for (a) $\sigma = 1$, (c) $\sigma = 15$.

It is the threshold which has the best mean contrast along the associated border $F(s_0)$. Instead of using this method to binarize images, we use it to measure the contrast locally. The evaluated contrast equals $2C(s_0)$ along the associated border $F(s_0)$. Finally, if $2C(s_0) > 5\%$, $F(s_0)$ is considered to be a visible edge. Details about the implementation of this method can be found in [26].

5.2.3 Noise robustness

The method derived from Köhler is robust to noise. We assume that the noise of the camera is gaussian.

Let consider two gaussian distributions of means L_1 and L_2 and standard deviations σ_1 and σ_2 . We can show that, as long as both distributions do not intersect, the optimal threshold s_0 found by Köhler's technique is a gaussian distribution with mean $\frac{L_1+L_2}{2}$ and standard deviation $\frac{1}{2}\sqrt{\sigma_1^2 + \sigma_2^2}$ [26].

Consequently, the method is robust to noise, because in average the returned threshold is the one without noise at the same distance of both distributions. This property is still verified when using the local formula of LIP contrast. Fig. 16 illustrates this property.

Figs. 16b and 16d are the same distributions with additive gaussian noise of standard

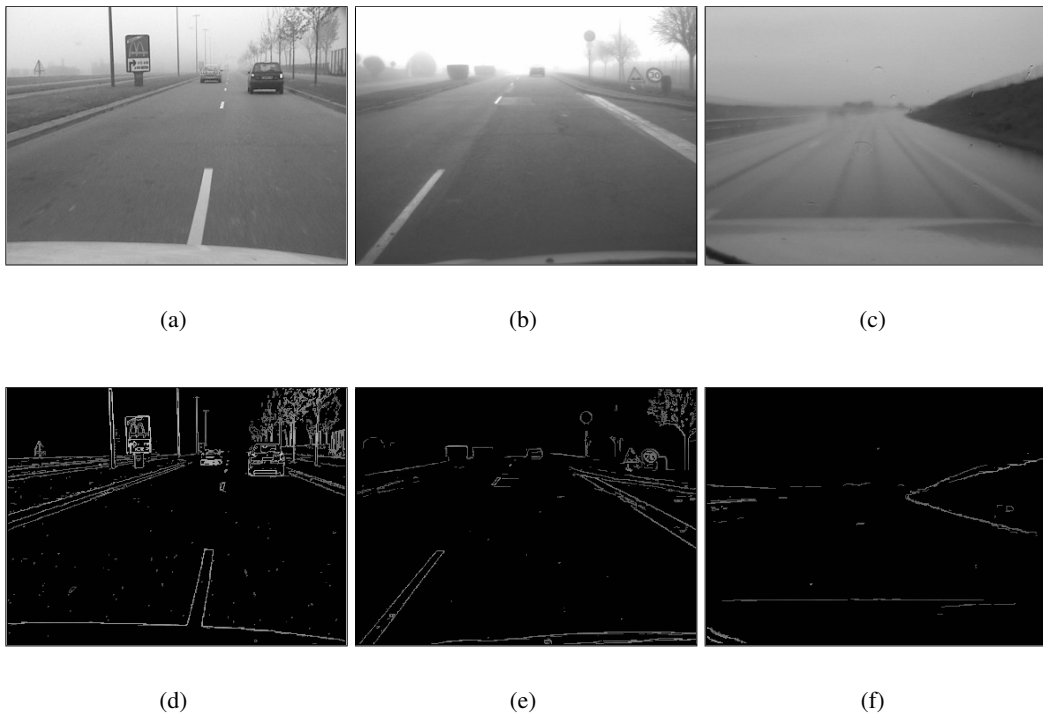


Figure 17: (a)(b)(c) Images grabbed under different meteorological conditions (light fog, dense fog, rain); (d)(e)(f) results of local contrasts above 5% computation.

deviation $\sigma = 1$ and $\sigma = 15$ respectively. The optimal threshold found by Köhler's technique, which is represented by the horizontal dashed line, is the same for both distributions. It is the one, which gives the maximum contrast (cf. Figs. 16b and 16d).

On the opposite, if both distributions are intersected, i.e. if $\max(3\sigma_1, 3\sigma_2) > \frac{L_2 - L_1}{2}$, Köhler's technique is not so efficient anymore.

5.2.4 Results samples

Some examples of computations of local contrast above 5% are given in Fig. 17 using images grabbed under different meteorological conditions.

5.3 Identifying a Suitable Telemetry

If just a single camera is used, we are unable to gain access to image depth, like it is depicted in Fig.18. This problem is generally overcome by adopting the hypothesis of a flat world, which makes it possible to associate a distance with each line of the image. However, the depth on vertical objects is incorrect and is unknown without another assumption. In a first

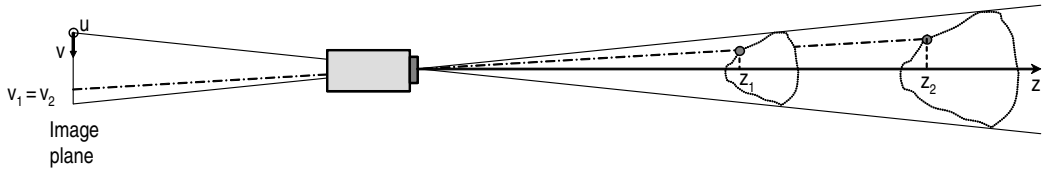


Figure 18: Principle of non-determination of depth using a single camera.

approach, we can detect picture elements belonging to the road surface. Techniques that search the road surface are numerous. A first family of methods finds the road surface by a segmentation process. Color segmentation [6, 33], texture segmentation [2] are the main approaches. A second family of methods finds the road surface by detection of its edges [3, 14, 58]. Conversely, we can detect the objects above the road surface. Some techniques are based on optic flow computation [21]. However, it is time consuming and the main hypothesis is not always verified (spatio-temporal luminous flow preserved). Some methods rely on template matching [4] or local symmetry [10] but are necessarily not generic. In addition, techniques like depth from scattering [48], depth from focus/defocus [19], shape from shading [62] are not adapted to our objectives.

We have developed a generic monocular approach. Knowing precisely the relative motion of the vehicle between two instants, the road plane in successive images is aligned, like in [55]. By perspective projection, the objects belonging to the road surface are correctly aligned, whereas the vertical objects are deformed. This allows estimating the mobilized visibility distance. The principle of this approach is presented in section 5.4.

If we use stereovision, we are not limited to the flat world hypothesis and we are able to gain access to the depth of nearly every pixels in the image [15]. However, because of real-time constraints, most approaches compute a sparse disparity map. We present our approach in section 5.5 which is based on "v disparity" concept [40]. Another approach based on "v-disparity" can be found in [57].

5.4 Generic Monocular Approach

5.4.1 Disparity Map Construction by Successive Images Alignment

Camera Model The different camera parameters were described in section 4.1. The transformation between the vehicle frame (with origin at the center of gravity of the vehicle) and the camera frame, is represented by a vectorial translation $\vec{t} = d\vec{X} + h\vec{Z}$ (see Fig. 19) and a rotation around the axes Y of angle β . We denote T the translation matrix and R the rotation matrix. The coordinate change between the image frame and the camera frame can be expressed using a projective matrix M_{proj} [34]:

$$M_{proj} = \begin{pmatrix} u_0 & 0 & -\alpha & 0 \\ v_0 & -\alpha & 0 & 0 \\ 1 & 0 & 0 & 0 \end{pmatrix} \quad (43)$$

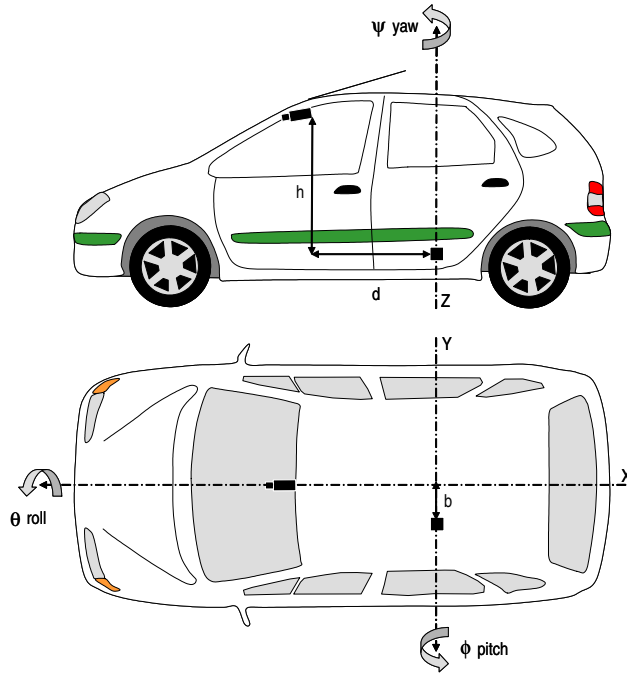


Figure 19: Position of the camera and vehicle dynamics.

At last, we obtain the transformation matrix T_r from the vehicle frame to the image frame:

$$T_r = M_{proj}RT \quad (44)$$

If P is a point with homogeneous coordinates $(X, Y, Z, 1)$ in the vehicle frame, its homogeneous coordinates in the image frame become:

$$p = T_r P = (x, y, z)^T \quad (45)$$

We can now compute the coordinates (u, v) of the projection of P in the image frame:

$$\begin{cases} u = \frac{x}{z} = u_0 + \alpha \frac{\cos \beta(Z + h) - \sin \beta(X + d)}{\cos \beta(X + d) + \sin \beta(Z + h)} \\ v = \frac{y}{z} = v_0 - \alpha \frac{Y}{\cos \beta(X + d) + \sin \beta(Z + h)} \end{cases} \quad (46)$$

Flat World Assumption If we consider I_1 and I_2 images taken at time t_1 and t_2 , the knowledge of the vehicle dynamics allows us, thanks to (46), to obtain an estimation of the image I_2 from the image I_1 . Let \tilde{I}_{12} be this estimated image and P a point whose projection in the image frame belongs to it. Let us assume that this point belongs to the road plane, meaning that if (X_2, Y_2, Z_2) are the coordinates of this point in the vehicle frame, then

$Z_2 = 0$. So the expression of X_2 and Y_2 is deduced from (46):

$$\begin{cases} X_2 = \frac{\cos \beta [d(u - u_0) + \alpha h] + \sin \beta [h(u - u_0) - \alpha d]}{\alpha \sin \beta - \cos \beta (u - u_0)} \\ Y_2 = \frac{-h(v - v_0)}{\alpha \sin \beta - \cos \beta (u - u_0)} \end{cases} \quad (47)$$

Vehicle Motion The motion M of the camera between two instants can be represented by a rotation and a translation. These transformations are in fact the same as the vehicle gets between two instants. Let ϕ be the yaw angle, ψ be the pitch angle and θ the roll angle (Fig. 19), then the rotation matrix Rot is given by:

$$Rot = \begin{pmatrix} \cos \phi \cos \psi & -\sin \psi \cos \theta + \cos \psi \sin \theta \sin \phi & \sin \psi \sin \theta + \cos \psi \cos \theta \sin \phi \\ \cos \phi \sin \psi & \cos \psi \cos \theta + \sin \psi \sin \theta \sin \phi & -\cos \psi \sin \theta + \sin \psi \cos \theta \sin \phi \\ -\sin \phi & \sin \theta \cos \phi & \cos \theta \cos \phi \end{pmatrix} \quad (48)$$

The translation can be decomposed following the axes X, Y, Z and is denoted $Trans = (T_x, T_y, T_z)^T$. The rotation-translation can be rewritten in terms of homogeneous coordinates with the following system:

$$\begin{pmatrix} X_2 \\ Y_2 \\ Z_2 \\ 1 \end{pmatrix} = \begin{pmatrix} Rot^T & T_x \\ & T_y \\ & T_z \\ 0 & 1 \end{pmatrix} \begin{pmatrix} X_1 \\ Y_1 \\ Z_1 \\ 1 \end{pmatrix} \quad (49)$$

Creation of an Aligned Image From the knowledge of the coordinates of a point P in (47) and of the vehicle dynamics given by M , we can express the coordinates of the point P in the camera frame at time t_1 :

$$(x_{12}, y_{12}, z_{12})^T = T_r M(X_2, Y_2, 0)^T \quad (50)$$

where M is the vehicle rotation/translation matrix. We obtain the coordinates (u_{12}, v_{12}) of P in the image frame of I_1 :

$$u_{12} = \frac{x_{12}}{z_{12}} \quad \text{and} \quad v_{12} = \frac{y_{12}}{z_{12}} \quad (51)$$

An example of aligned image computation for a large displacement ($\approx 4m$) is shown in Fig. 20.

5.4.2 Pseudo-Disparity Map Computation

Image Matching We have to match both images I_1 and \tilde{I}_{12} . It means that we have to find local correspondences between two neighborhoods from each image. These correspondences are computed via the ZNCC correlation metrics (a comparison of different existing metrics is carried out in [50]):

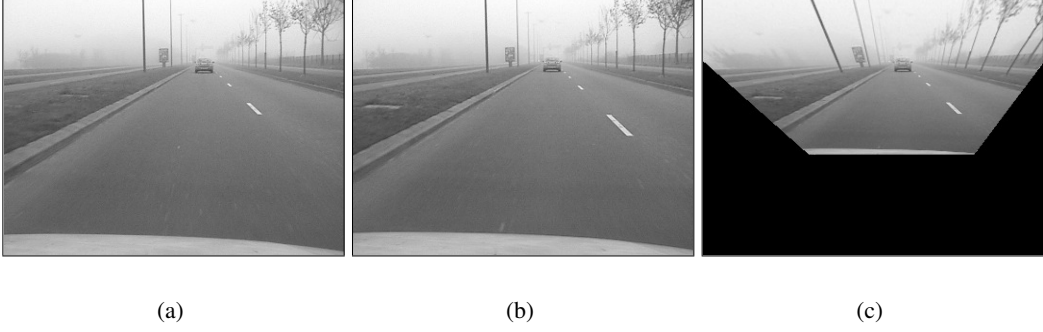


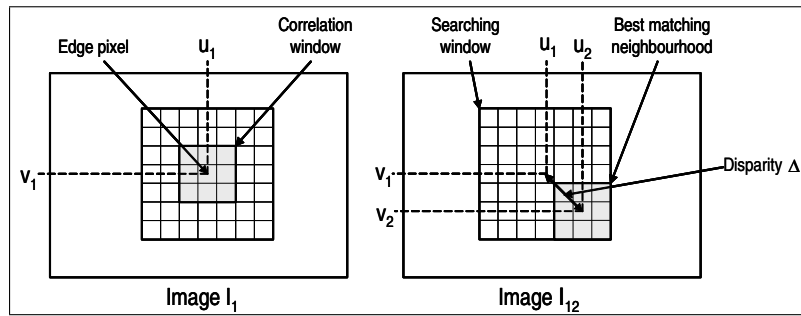
Figure 20: (a) Image I_1 ; (b) image I_2 ; (c) aligned image \tilde{I}_{12} for a big displacement ($\approx 4m$).

$$\frac{\sum_i \left(I_1(x+i) - \bar{I}_1(x) \right) \left(\tilde{I}_{12}(x+\Delta+i) - \bar{\tilde{I}}_{12}(x+\Delta) \right)}{\sqrt{\sum_i \left(I_1(x+i) - \bar{I}_1(x) \right)^2 \sum_i \left(\tilde{I}_{12}(x+\Delta+i) - \bar{\tilde{I}}_{12}(x+\Delta) \right)^2}} \quad (52)$$

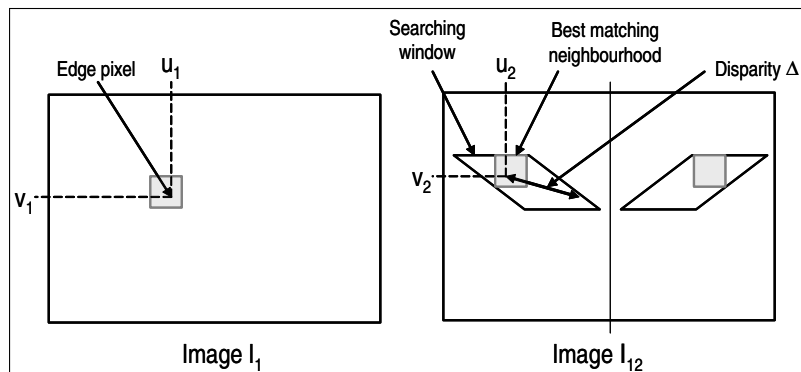
where $\bar{I}_1(x)$ and $\bar{\tilde{I}}_{12}(x+\Delta)$ are the means of pixel intensities for the window centered at x and Δ is the considered shift.

The more the correlation score is close to 1, the more we can consider these two neighborhoods as identical. Since the road plane is aligned in both images I_1 and \tilde{I}_{12} , no scanning is normally necessary to match image features using $ZNCC$ correlation. However, working on a single pair of neighborhoods limits our study. Indeed, some matching errors can occur and a pixel belonging to the road can be incorrectly aligned in the image \tilde{I}_{12} . That's why we defined a search window (cf. Fig. 21a). The correlation neighborhood in image I_1 is centered on an edge pixel. The correlation neighborhood in the image \tilde{I}_{12} is centered successively around a pixel varying in a search neighborhood centered on the pixel (u_1, v_1) in image I_1 .

We defined two kinds of search neighborhoods: squared neighborhoods for objects belonging to the road plane and deformed neighborhoods for vertical objects (cf. Fig. 21, like it is done in spatial stereovision [59]). Indeed, one can notice that objects not belonging to the road plane are deformed towards the top and the borders of the image after image alignment. Finally, the idea is to compute for each pixel of gradient a disparity with a normal and a deformed searching neighborhood and to keep the disparity giving the best $ZNCC$ correlation score. An example of result is given in Fig.22 using actual images of fog. The majority of pixels belonging to the road plane is successfully recognized, contrary to the pixels belonging to the vertical sign. Having now the pixels belonging to the road plane, we can associate a depth with each line of the image assuming a flat world using (13). In this process, we do not necessary need to find the pixels belonging to the vertical objects. However, they are used to filter erroneous pixels associated to the road plane or to



(a)



(b)

Figure 21: (a) Correlation neighborhood and search window; (b) Correlation with deformed window for the non-road hypothesis.

a vertical object according the majority of pixels found in a neighborhood.

Details about the method implementation as well as the role that plays the vehicle dynamics in the method are given in [9].

5.5 Generic Binocular Approach

The previous method is able to compute a depth map of the road surface using a single camera coupled an inertial navigation system. However, we have to assume that the road is flat. The mobilized visibility distance is thus the range to the most distant visible object on the road plane. In this section, we use spatial stereovision and we are thus able to compute the road profile. The mobilized visibility distance will thus be the range to the most distant visible object on the road surface. From a theoretical point of view, the method should be

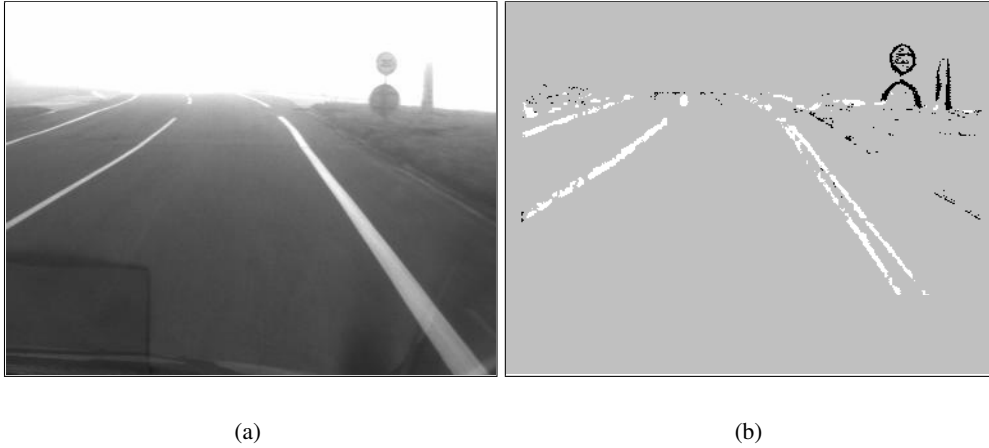


Figure 22: (a) Fog image taken by the onboard camera. (b) In white: points belonging to the road plane. In black: points not belonging to the road plane.

more precise since the road is never a perfect plane. However, it requires a stereovision sensor with a rectified epipolar geometry which is also a rather strong constraint.

5.5.1 The Image of a Plane in the "v-disparity" Image

The stereovision algorithm uses the "v-disparity" transform, in which the detection of straight lines is equivalent to the detection of planes in the scene. In this aim, we represent the v coordinate of a pixel towards the disparity Δ (performing accumulation from the disparity map along scanning lines) and detect straight lines and curves in this "v-disparity" image (denoted by $I_{v\Delta}$) [40].

This algorithm assumes the road scene is composed of set of planes: obstacles are modeled as vertical planes, whereas the road is supposed to be an horizontal plane (when it is planar), or a set of oblique planes (when it is not planar), as shown in Fig. 23.

According to the modeling of the stereo sensor given on Fig. 23, the plane of equation $Z = d$, corresponding to a vertical object, is projected along the straight line of (53) in $I_{v\Delta}$:

$$\Delta = \frac{b}{d}(v - v_0) \sin \theta + \frac{b}{d}\alpha \cos \theta \quad (53)$$

The plane of equation $Y = 0$, corresponding to the road surface, is projected along the straight line of (54) in $I_{v\Delta}$:

$$\Delta = \frac{b}{h}(v - v_0) \cos \theta + \frac{b}{h}\alpha \sin \theta \quad (54)$$

The different camera parameters were described in section 4.1. The other parameters

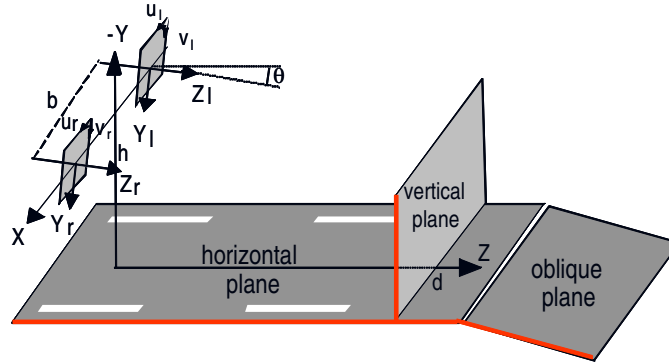


Figure 23: Domain of validity of the study and coordinate systems used.

are h which denotes the height of the cameras above the ground and b which is the distance between the cameras (i.e. the stereoscopic base). Details can be found in [40].

5.5.2 "V-disparity" Image Construction and 3D Surface Extraction

The algorithm performs a robust extraction of these planes from which it deduces many useful information about the road and the obstacles located on its surface. Fig. 28 illustrates the outline of the process. From two stereo images, a disparity map I_{Δ} is computed (ZNCC criteria is used to this purpose along edges). Then an accumulative projection of this disparity map is performed to build the "v-disparity" image $I_{v\Delta}$. For the image line i , the abscissa u_M of a point M in $I_{v\Delta}$ corresponds to the disparity Δ_M and its grey level i_M to the number of points with the same disparity Δ_M on the line i : $i_M = \sum_{P \in I_{\Delta}} \delta_{v_P, i} \delta_{\Delta_P, \Delta_M}$ where $\delta_{i,j}$ denotes the Kronecker delta. From this "v-disparity" image, a robust extraction of straight lines is performed through a Hough transform. This extraction of straight lines is equivalent to the extraction of the planes of interest taken into account in the modeling of the road scene (see Fig. 24c).

5.5.3 Disparity Map Improvement

Sparse approach In order to quickly compute the "v-disparity" image, a sparse and rough disparity map has been built. This disparity map may contain numerous false matches, which prevents us to use it as a depth map of the environment. Thanks to the global surfaces extracted from the "v-disparity" image, false matches can be removed. In this aim, we check whether a pixel of the disparity map belongs to any global surface extracted using the same matching process. If it is the case, the same disparity value is mapped to the pixel and leads to Fig. 24d. Details of this process can be found in [39]. Finally, this enhanced disparity map can be used as a depth map of the vehicle environment, since the depth D of a pixel of disparity Δ is expressed by:

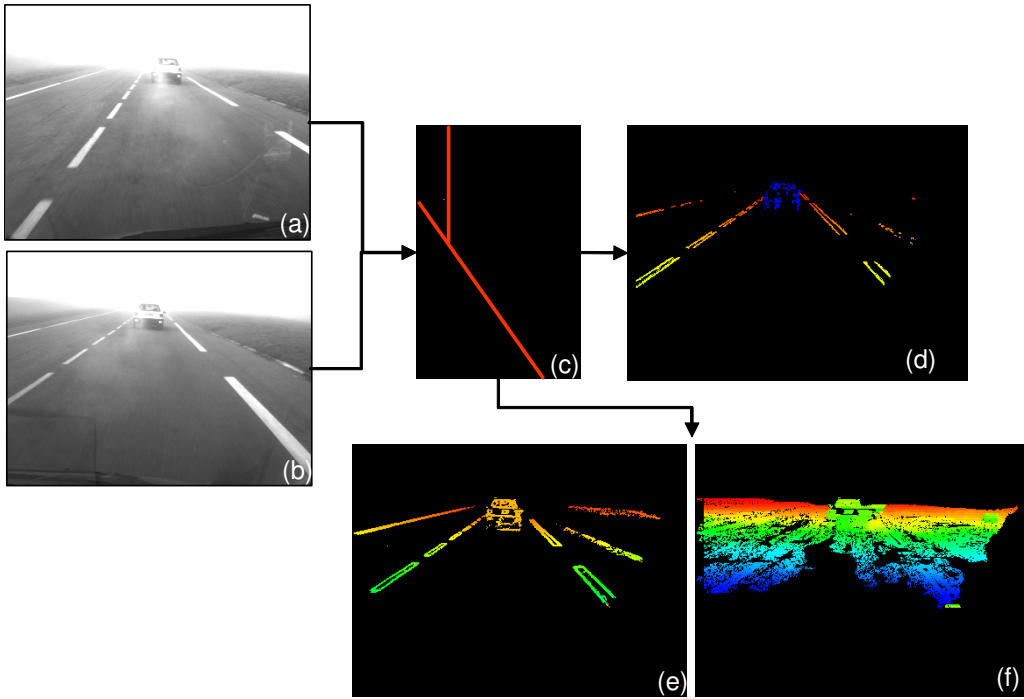


Figure 24: Overview of two steps "v-disparity" approach using on a foggy stereo pair of images: (a) left image; (b) right image; (c) "v-disparity" image computed using (a) and (b) images; (d) improved sparse disparity map; (e) (f) samples of improved quasi-dense disparity maps.

$$D = \frac{b(\alpha \cos \theta - (j - v_0) \sin \theta)}{\Delta} \quad (55)$$

Quasi-dense approach However, such a disparity map is sparse, i.e. the disparity is known only on vertical edges pixels. But under degraded weather conditions, it poses a problem, particularly on the top of vertical objects, such as vehicles where numerous false matches still exist.

To cope with this situation, a complementary approach has been proposed. It is based on a disparity propagation method.

We thus propagate the seeds, which are the set of the matched pixels in the first pass of the v-disparity algorithm, like in [43], except that for each matching pair candidate, we check if it belongs to one the profiles of the v-disparity image. Thanks to this approach, the disparity map is quasi-dense especially on the horizontal edges (see Figs. 24ef). Compared to dense disparity matching approaches, the computation of these disparity maps is rather low cost in terms of computation time and allows to precisely locate some bounding boxes

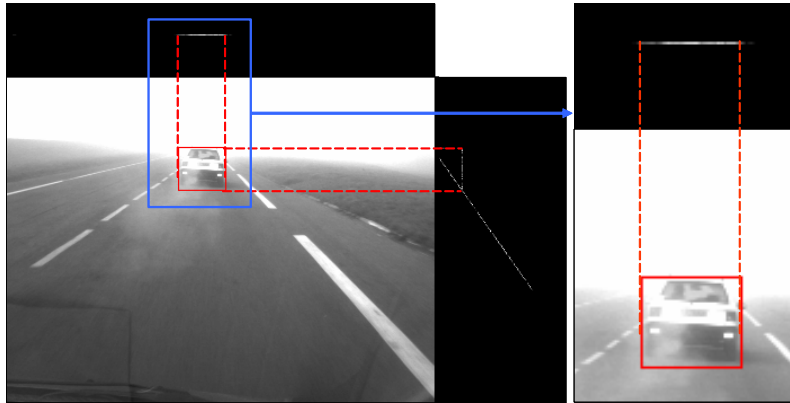


Figure 25: Example of a bounding box around a vehicle in foggy weather. Although the vehicle is not well contrasted and can be confused with the sky, an accurate bounding box is provided.

around vertical objects using "u-disparity" approach [29], like in Fig. 25.

5.6 Real-time Disparity Contrast Combination

To estimate the visibility distance, we have now to combine a disparity map of the road surface obtained using one of the previously described approaches with a contrast map. Because most distant objects on the road plane are on the horizon line, the scanning starts from this location. Within each neighborhood where a point of disparity is known the contrast is computed. The process stops when a contrast above 5% is met. The visibility distance is then the depth of the picture element with a contrast above 5%. This generic process has been patented [27].

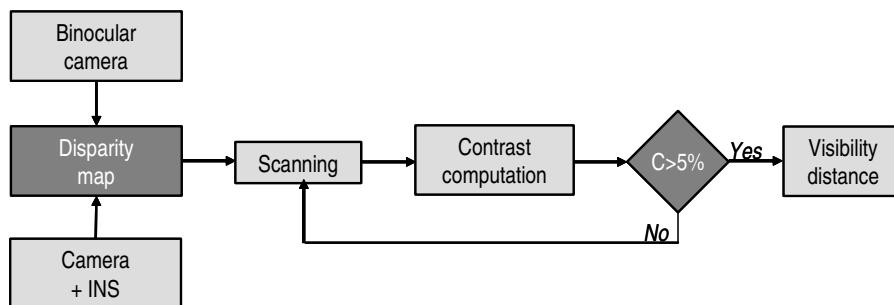


Figure 26: Overview of the real-time disparity contrast combination algorithm.

5.7 Results

An example of final result is given in Fig. 27. In Fig. 27a, the result of local contrasts above 5% is presented for a daytime foggy weather image. In Fig. 27b, the final result of the algorithm is shown. In particular, the disparity point, on which the visibility distance is computed, is represented with a black cross inside the white window.

Finally, Figs. 28 and 29 show some results of mobilized visibility distance computations using stereovision in two fog video sequences (daytime and twilight fog) [28].

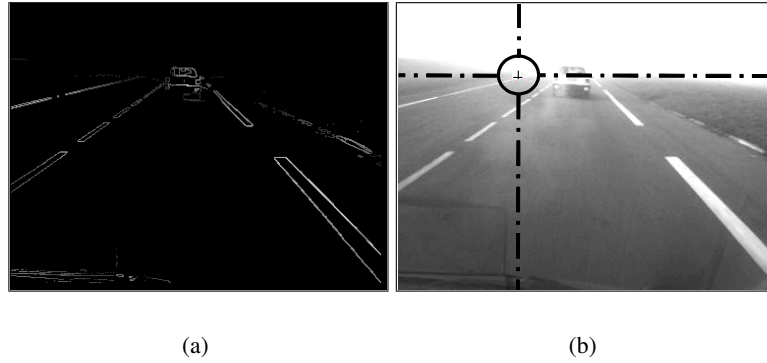


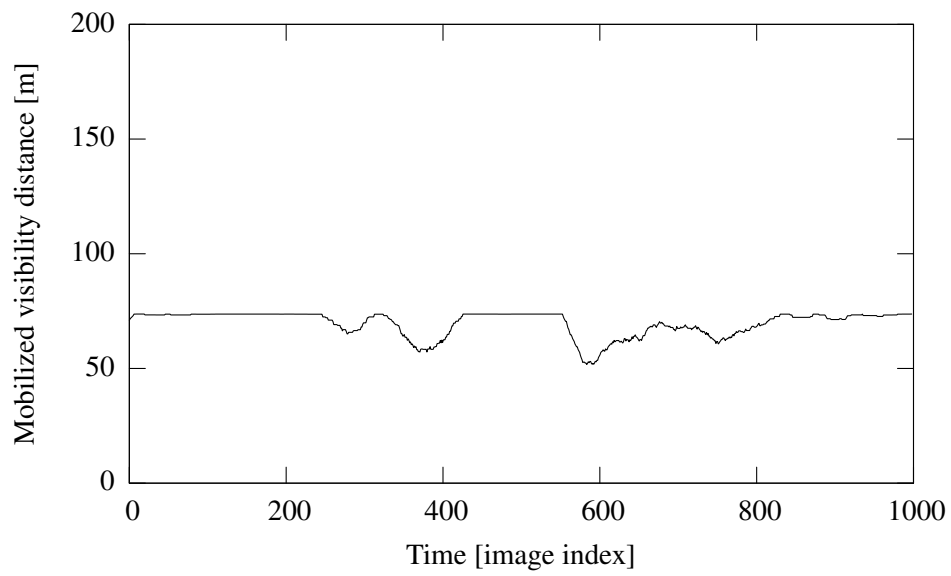
Figure 27: Final result: the most distant window with a contrast above 5 %, on which a point of disparity is known, is the circle. The disparity point is represented with a black cross inside the white window. (a) local contrasts above 5%; (b) foggy weather ($V_{mob} \approx 75m$).



(a)

(b)

(c)



(d)

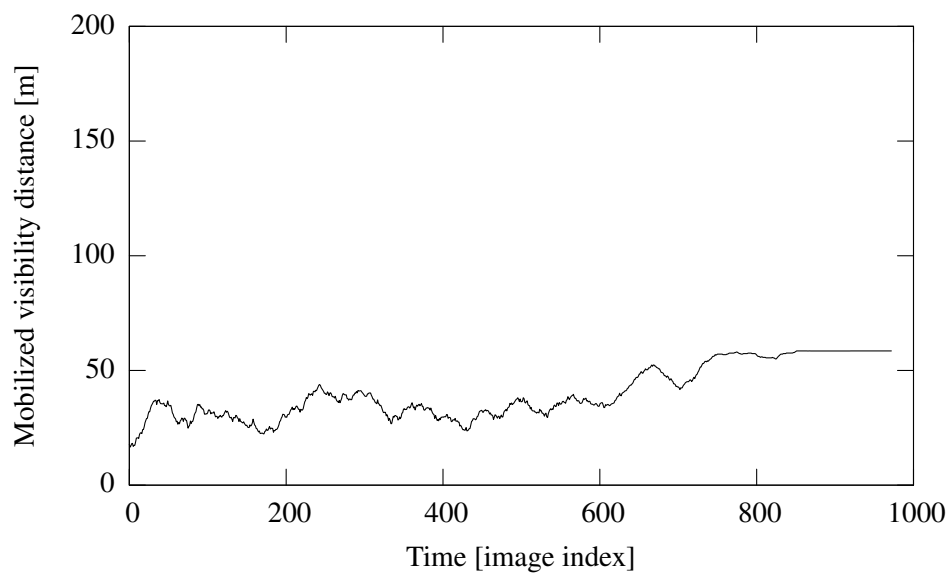
Figure 28: (d) Plot of the mobilized visibility distance estimation using stereovision based on the daytime fog video sequence illustrated in (a)(b)(c).



(a)

(b)

(c)



(d)

Figure 29: (d) Plot of the mobilized visibility distance estimation using stereovision based on the twilight fog video sequence illustrated in (a)(b)(c).

6 Contrast Restoration of Fog Degraded Images

Once visibility distance has been determined, it can be used to adjust some parameters in other image processing algorithms. This section is devoted to such an application focusing on contrast restoration.

According to (5), the contrast of images is drastically degraded and varies across the scene under daytime foggy weather. Consequently, advanced driver assistances relying on artificial vision and pattern analysis are no longer able to run properly. To mitigate this problem, we proposed to restore the contrast by inverting Koschmieder's Law to recover the value of the intrinsic intensity R at each point of the scene, such as:

$$R = Ie^{kd} + A_\infty [1 - e^{kd}] \quad (56)$$

Then, according to the strategy used to approximate the depth distribution d of the road scene, different applications can be constructed.

6.1 Contrast Restoration of the Road Surface

Road departure prevention is usually based on a lane marking detector relying on a single camera mounted behind the windshield of the vehicle. In these conditions, most systems assume a flat road. This assumption can also be used to restore the contrast of the road surface. Thus, using (18) and (56), one obtains:

$$\begin{cases} R = Ie^{2\frac{v_i - v_h}{v - v_h}} + A_\infty [1 - e^{2\frac{v_i - v_h}{v - v_h}}] \\ A_\infty = I_i + \frac{(v_i - v_h)}{2} \frac{\partial I}{\partial v} \Big|_{v=v_i} \end{cases} \quad (57)$$

Details of the method are given in [24]. To illustrate the algorithm, the lane markings have been extracted in a foggy image with and without contrast restoration using the method described in [56] with the same setting (see Fig. 30). One can see that the operation range of the lane marking detector is enhanced thanks to the contrast restoration process.

6.2 Contrast Restoration of the Road Scene

To restore the contrast of the road scene and not only the contrast of the road surface, another approach is proposed. In this context, the depth distribution in the scene can be roughly modeled in two parts. A first part models the road surface which can be approximated by a plane like in the previous paragraph. A second part models the objects above the road surface. According to classical perspective geometrical representations, the depth of a scene point can be expressed as a function of the euclidian distance in the image plane between the corresponding pixel and the vanishing point (u_h, v_h) [47]. Consequently, the depth d of a pixel with (u, v) coordinates can be inferred as:

$$d = \min \left[\frac{\lambda}{v - v_h}, \frac{\kappa}{\sqrt{(u - u_h)^2 + (v - v_h)^2}} \right] \quad (58)$$

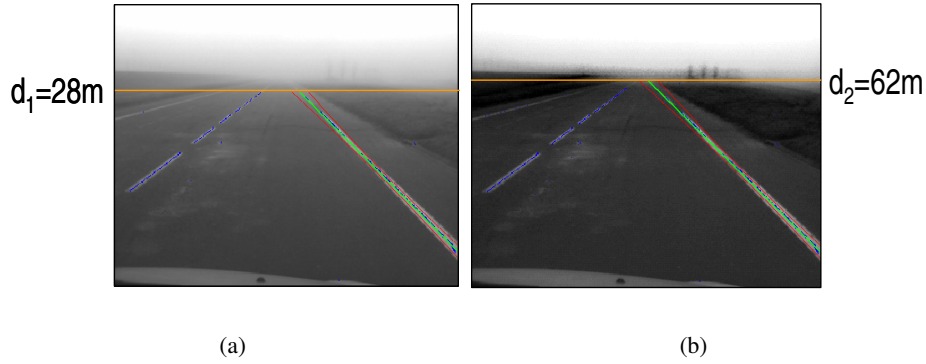


Figure 30: (a) Original foggy image used for lane markings detection using the method described in [56]; (b) image with restored contrast used for lane markings detection using the same parameters as the first image, i.e. a gradient threshold of 10 (blue: pixels likely to be lane markings, green: fitted lane marking, red: level of confidence on the fitting).

where $\kappa > l$ models the relative importance of the flat world against the vertical world. To correctly restore the contrast, according to the scene model given in the previous paragraph, the remaining task consists in finding the optimal values of κ and c . To do it, one solution is to solve the following equation using Powell's method:

$$(\kappa^*, c^*) = \underset{\substack{\kappa > 1 \\ c > 0}}{\operatorname{argmax}} \left[Q(\kappa, c) + \kappa - c \right] \quad (59)$$

where c is a parameter which defined a clipping plane at $d = \frac{\lambda}{c - v_h}$ which is used to limit the depth modeling errors near the horizon line and Q is a norm of the local normalized correlation between the original image and the restored image. Indeed, the *normalized* correlation score between the original and the restored versions of a neighborhood should remain high. A decreasing normalized correlation means that the content of the original and restored neighborhoods differ. More details about this method are given in [31]. Sample results are given in Fig. 31.

6.3 Simultaneous Contrast Restoration and Obstacle Detection

Initialized with a small initial value of κ in (58), e.g. $\kappa = 1.1\lambda$, the principle of the simultaneous contrast restoration and obstacle detection algorithm is to progressively increase the value of κ and to detect the distorted areas. As soon as vertical objects are encountered, a local contrast distortion can be noticed. In this case, the vertical object causing the distortion is detected by "u-v disparity" stereovision approach, detailed in paragraph 5.5. The increase of κ can then be restarted until the desired final value, e.g. $\kappa = 10\lambda$, is reached. The algorithm is detailed in [30] and illustrated in Fig. 32.



Figure 31: Example of contrast restoration of a road scene. (a) Original image. (b) Image with restored contrast. In the white circle, the second car that appears in the restored image.

In this way, scattering is turned to our advantage allowing us to detect vertical objects, which can then be confirmed by another approach (stereovision in this case). Based on this principle, we plan to develop such novel algorithms aiming at recovering the third dimension of scenes using a single image by exploiting the scattering of the light by atmospheric particles.

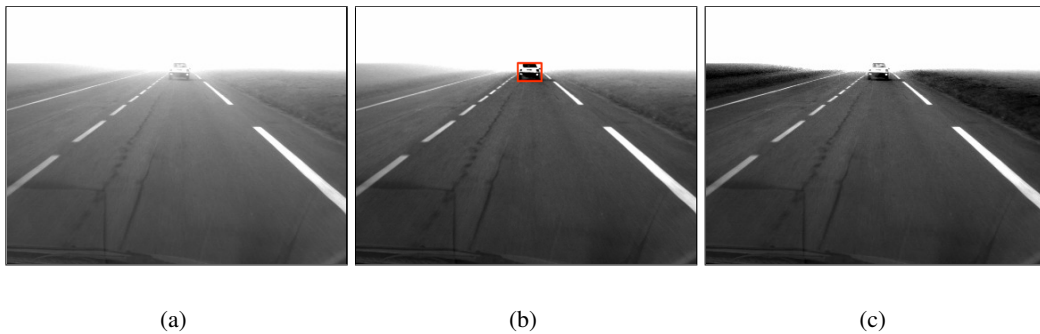


Figure 32: (a) original foggy image; (b) image with half restored contrast and a bounding around the detected obstacle; (c) image with full restored contrast.

7 Discussion and Perspectives

In the previous sections, an approach to deal with adverse visibility conditions in daytime fog was presented: modeling, methods, experimental validation and applications. Admit-

tedly there is still some work ahead to finalize and validate the applications, in a near future we would like to tackle other adverse meteorological or lighting conditions: night-time fog (Fig. 33c), rain (Fig. 33a), sun at grazing angle (Fig. 33b), snow fall, entrance or exit of tunnels, even though existing works on these subjects are quite rare. Consequently, to be able to develop new methods and applications, a lot of work is needed to model, simulate or reproduce these adverse conditions.

However, as mentioned in the introduction, it is one of the keys to obtain a very important level of reliability of the sensor unit inside the vehicles and associated signal processing. Then, new systems for the vehicle using a camera could be developed. It would lead to increase the number of supported functions by the camera (rain sensor, fog sensor, etc.) and thus to reduce the cost of its installation in future vehicles. In this way, the deployment of such onerous systems could be facilitated.

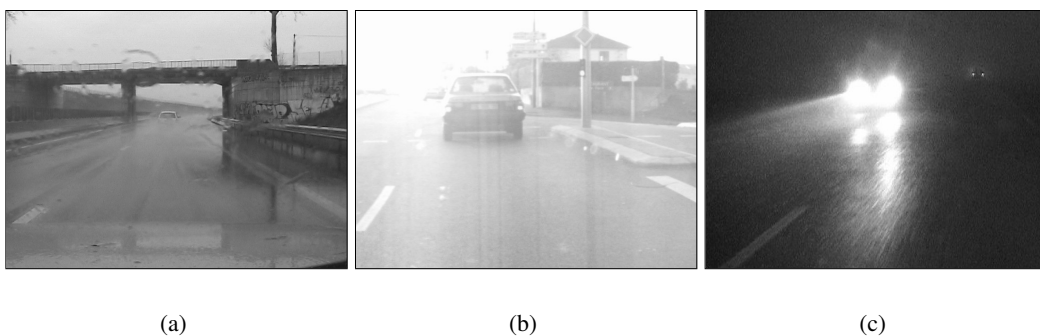


Figure 33: (a) rainy weather; (b) sun at grazing angle; (c) night-time fog situation.

8 Conclusion

In this chapter, methods have been presented to deal with daytime fog conditions in the future driver assistances using optical sensors. First of all, a daytime fog modeling has been recalled and new visibility distances have been proposed fitting well with these driving conditions. Two complementary methods have been presented aiming at estimating the visibility range using respectively one or two onboard cameras. Both methods are based on the definition of the meteorological visibility distance. The first technique, using a model of atmospheric scattering, detects and estimates the density of daytime fog by using a single camera. The second technique, using a generic property of the atmosphere, is able to estimate the visibility range under all meteorological conditions both in daytime and in night time by using a stereoscopic sensor or a single camera coupled with an inertial navigation system. In the future, these methods are likely to be used to provide drivers with an appropriate speed with respect to the visibility range, or to automate the fog lamps. Once the

weather conditions have been determined, they can have been exploited to reduce the impact of adverse weather conditions on the operation of vision systems. We have thus proposed different solutions to enhance the performances of vision algorithms under foggy weather. Finally, we have tackled the problem to know if light scattering could be turned to our advantage, allowing us to develop novel perception algorithms. Methods are validated using actual fog images grabbed under various situations on the test track of Versailles Satory in France. In the future, we would like to apply this approach to other adverse conditions like night-time fog, rain, low angled sun, etc.

References

- [1] E. Allard. *Mémoire sur l'intensité et la portée des phares*. 1876.
- [2] R. Aufrère, R. Chapuis, and F. Chausse. A fast and robust vision algorithm to locate a vehicle on a non-structured road. *International Journal of Robotics Research*, 19(5):411–423, May 2000.
- [3] M. Bertozzi, A. Broggi, M. Cellario, A. Fascioli, and M. Porta. Artificial vision in road vehicles. *Proceedings of the IEEE - Special issue on Technology and Tools for Visual Perception*, 90(7):1258–1271, 2002.
- [4] M. Betke and H. Nguyen. Highway scene analysis from a moving vehicle under reduced visibility conditions. In *IEEE Intelligent Vehicles Symposium, Stuttgart, Germany*, volume 1, pages 131–136, October 1998.
- [5] P. Bhartia and I.J. Bahl. *Millemeter Wave Engineering and Applications*. John Wiley and Sons, 1984.
- [6] E. Bigorgne and J.-P. Tarel. Backward segmentation and region fitting for geometrical visibility range estimation. In *Asian Conference on Computer Vision, Tokyo, Japan*, November 2007.
- [7] C. Boehlau. Optical sensors for AFS - supplement and alternative to GPS. In *Progress in Automotive Lighting Symposium, Darmstadt, Germany*, September 2001.
- [8] P. Bouguer. *Traité d'optique sur la gradation de la lumière*. 1729.
- [9] C. Boussard, N. Hautière, and B. d'André Novel. Vision guided by vehicle dynamics for onboard estimation of the visibility range. In *IFAC Symposium on Intelligent Autonomous Vehicles, Toulouse, France*, September 3-5 2007.
- [10] A. Broggi, A. Fascioli, C. G. L. Bianco, and A. Piazzzi. Visual perception of obstacles and vehicles for platooning. *IEEE Transactions on Intelligent Transportation Systems*, 1(3):164–176, 2000.

-
- [11] R. Brown. A new lidar for meteorological application. *Journal of Applied Meteorology*, 12(4):698–708, 1973.
- [12] C. Bush and E. Debes. Wavelet transform for analyzing fog visibility. *IEEE Intelligent Systems*, 13(6):66–71, November/December 1998.
- [13] P. Carrea and A. Saroldi. Integration between anticollision and AICC functions: The ALERT project. In *Intelligent Vehicles Symposium, Tokyo, Japan*, July 1993.
- [14] R. Chapuis, R. Aufrère, and F. Chausse. Accurate road following and reconstruction by computer vision. *IEEE Transactions on Intelligent Transportation Systems*, 3(4):261–270, December 2002.
- [15] P. Charbonnier, V. Muzet, P. Nicolle, N. Hautière, J.-P. Tarel, and D. Aubert. La stéréovision appliquée à l'analyse de scènes routières. *submitted to Bulletin des Laboratoires des Ponts et Chaussées*, 2007.
- [16] CIE. *International Lighting Vocabulary*. Number 17.4. 1987.
- [17] R. Collis. Lidar. *Applied Optics*, 9(8):1782–1788, 1970.
- [18] M. Colomb *et al.* The main results of a european research project: "improvement of transport safety by control of fog production in a chamber" ("FOG"). In *International Conference on Fog, Fog Collection and Dew*, October 2004.
- [19] F. Deschênes and D. Ziou. Depth from defocus estimation in spatial domain. *Computer Vision and Image Understanding*, 81(2):143–165, February 2001.
- [20] E. Dumont and V. Cavallo. Extended photometric model of fog effects on road vision. *Transportation Research Records*, (1862):77–81, 2004.
- [21] U. Franke and C. Rabe. Kalman filter based depth from motion with fast convergence. In *IEEE Intelligent Vehicles Symposium, Las Vegas, USA*, pages 180–185, June 2005.
- [22] M.D. Grossberg and S. K. Nayar. Modelling the space of camera response functions. *IEEE Transactions on Pattern Analysis and Machine Intelligence*, 26(10):1272–1282, 2004.
- [23] N. Hautière and D. Aubert. Fog detection through use of a CCD onboard camera. *Ingénieurs de l'automobile*, (773):83–86, November-December 2004.
- [24] N. Hautière and D. Aubert. Contrast restoration of foggy images through use of an onboard camera. In *IEEE Conference on Intelligent Transportation Systems, Vienna, Austria*, pages 1090–1095, September 2005.
- [25] N. Hautière, D. Aubert, and E. Dumont. Mobilized and mobilizable visibility distances for road visibility in fog. In *26th Session of the CIE, Beijing, China*, July 2007.

- [26] N. Hautière, D. Aubert, and M. Jurlin. Measurement of local contrast in images, application to the measurement of visibility distance through use of an onboard camera. *Traitement du Signal*, 23(2):145–158, 2006.
- [27] N. Hautière, R. Labayrade, and D. Aubert. Dispositif de mesure de distance de visibilité. Brevet français No. 0411061 soumis par LCPC/INRETS, octobre 2004.
- [28] N. Hautière, R. Labayrade, and D. Aubert. Real-Time Disparity Contrast Combination for Onboard Estimation of the Visibility Distance. *IEEE Transactions on Intelligent Transportation Systems*, 7(2):201–212, June 2006.
- [29] N. Hautière, R. Labayrade, M. Perrollaz, and D. Aubert. Road scene analysis by stereovision: a robust and quasi-dense approach. In *IEEE International Conference on Automation, Robotics, Control and Vision, Singapore*, December 2006.
- [30] N. Hautière, J.-P. Tarel, and D. Aubert. Simultaneous contrast restoration and obstacles detection: First results. In *IEEE Intelligent Vehicles Symposium, Istanbul, Turkey*, pages 130–135, June 13-15 2007.
- [31] N. Hautière, J.-P. Tarel, and D. Aubert. Towards fog-free in-vehicle vision systems through contrast restoration. In *IEEE Computer Society Conference on Computer Vision and Pattern Recognition, Minneapolis, USA*, June 2007.
- [32] N. Hautière, J.-P. Tarel, J. Lavenant, and D. Aubert. Automatic fog detection and estimation of visibility distance through use of an onboard camera. *Machine Vision and Applications Journal*, 17(1):8–20, April 2006.
- [33] Y. He, Wang H., and B. Zhang. Color-based road detection in urban traffic scenes. *IEEE Transactions on Intelligent Transportation Systems*, 5(4):309–318, December 2004.
- [34] R. Horaud and O. Monga. *Vision par ordinateur, outils fondamentaux*. Editions Hermès, 1995.
- [35] M. Jurlin and J.-C Pinoli. Logarithmic image processing. *Advances In Imaging and Electron Physics*, 115:129–196, 2001.
- [36] R. Kurata, H. Watanabe, M. Tohno, T. Ishii, and H. Oouchi. Evaluation of the detection characteristics of road sensors under poor-visibility conditions. In *IEEE Intelligent Vehicles Symposium, Parma, Italy*, June 2004.
- [37] T. M. Kwon. Atmospheric visibility measurements using video cameras: Relative visibility. Technical report, University of Minnesota Duluth, July 2004.
- [38] R. Köhler. A segmentation system based on thresholding. *Graphical Models and Image Processing*, 15:319–338, 1981.

-
- [39] R. Labayrade and D. Aubert. In-vehicle obstacles detection and characterization by stereovision. In *First International Workshop on In-Vehicle Cognitive Computer Vision Systems, Graz, Austria*, April 2003.
- [40] R. Labayrade, D. Aubert, and J.-P. Tarel. Real time obstacle detection in stereovision on non flat road geometry through v-disparity representation. In *Proc. IEEE Intelligent Vehicles Symposium*, June 2002.
- [41] J. Lavenant, J.-P. Tarel, and D. Aubert. Procédé de détermination de la distance de visibilité et procédé de détermination de la présence d'un brouillard. Brevet français 0201822 soumis par LCPC / INRETS, Février 2002.
- [42] LCPC, editor. *bulletin de liaison des laboratoires des Ponts et Chaussées*, volume Hors série thématique : visibilité, Février 1993.
- [43] M. Lhuillier and L. Quan. Match propagation for image-based modeling and rendering. *IEEE Transactions on Pattern Analysis and Machine Intelligence*, 24(8):1140–1146, 2002.
- [44] J.L. Mannos and D.J. Sakrison. The effects of visual fidelity criterion on the encoding of images. *IEEE Transactions on Information Theory*, IT-20(4):525–536, 1974.
- [45] W.E.K. Middleton. *Vision through the atmosphere*. University of Toronto Press, 1952.
- [46] M. Minnaert. *The Nature of Light and Color in the Open Air*. 1954.
- [47] S. G. Narashiman and S. K. Nayar. Interactive deweathering of an image using physical model. In *IEEE Workshop on Color and Photometric Methods in Computer Vision*, October 2003.
- [48] S. G. Narasimhan and S. K. Nayar. Contrast restoration of weather degraded images. *IEEE Transactions on Pattern Analysis and Machine Intelligence*, 25(6):713–724, June 2003.
- [49] T. Ogawa and K. Takagi. Lane recognition using on-vehicle lidar. In *IEEE Intelligent Vehicles Symposium, Tokyo, Japan*, June 13-15 2006.
- [50] M. Perrollaz. Construction d'une carte de disparité et application à la detection d'obstacles routiers. 2006. Technical Report, INRETS/LCPC.
- [51] M. Perrollaz, R. Labayrade, C. Royère, N. Hautière, and D. Aubert. Long range obstacle detection using laser scanner and stereovision. In *IEEE Intelligent Vehicles Symposium, Tokyo, Japan*, pages 182–187, June 13-15 2006.
- [52] D. Pomerleau. RALPH: Rapidly adapting lateral position handler. In *IEEE Intelligent Vehicles Symposium, Detroit, USA*, September 1995.

- [53] D. Pomerleau. Visibility estimation from a moving vehicle using the RALPH vision system. In *IEEE Conference on Intelligent Transportation Systems, Boston, USA*, November 1997.
- [54] F. Rosenstein. Intelligent rear light - constant perceptibility of light signals under all weather conditions. In *International Symposium on Automotive Lighting, Darmstadt, Germany*, pages 403–414, September 2005.
- [55] G.-P. Stein, P. Mano, and A. Shashua. A robust method for computing vehicle ego-motion. In *IEEE Intelligent Vehicles Symposium*, october 2000.
- [56] J.-P. Tarel, S.-S. Ieng, and P. Charbonnier. Using robust estimation algorithms for tracking explicit curves. In *European Conference on Computer Vision, Copenhagen, Denmark*, May 2002.
- [57] J.-P. Tarel, S.-S. Ieng, and P. Charbonnier. Accurate and robust image alignment for road profile reconstruction. In *IEEE International Conference on Image Processing, San-Antonio, Texas, USA*, September 2007.
- [58] J.-P. Tarel, S.-S. Ieng, and P. Charbonnier. Robust lane marking detection by the half quadratic approach. In *Etudes et Recherches des Laboratoires des Ponts et Chaussées*. 2007.
- [59] Todd A. Williamson. *A High-Performance Stereo Vision System for Obstacle Detection*. PhD thesis, Carnegie Mellon University, september 1998.
- [60] S. Winkler. Issues in vision modeling for perceptual video quality assessment. *Signal Processing*, 78(2):231–252, october 1999.
- [61] G. Yahiaoui and P. Da Silva Dias. In board visibility evaluation for car safety applications: a human vision modelling based approach. In *ITS World Congress, Madrid, Spain*, November 2003.
- [62] R. Zhang, P.-S. Tsai, J. E. Cryer, and M. Shah. Shape from shading: A survey. *IEEE Transactions on Pattern Analysis and Machine Intelligence*, 21(8):690–706, August 1999.